Tutorial: Metalorganic Chemical Vapor Deposition of β-Ga_2O_3 thin films, alloys and heterostructures

A F M Anhar Uddin Bhuiyan[1,*], Zixuan Feng[1], Lingyu Meng[1], and Hongping Zhao[1,2,‡]

[1]Department of Electrical and Computer Engineering, The Ohio State University, Columbus, OH 43210, USA

[2]Department of Materials Science and Engineering, The Ohio State University, Columbus, OH 43210, USA

[*]Email: bhuiyan.13@osu.edu [‡]Corresponding author Email: zhao.2592@osu.edu

β-phase gallium oxide (Ga_2O_3) is an emerging ultrawide bandgap (UWBG) semiconductor with bandgap energy of ~ 4.8 eV and predicted high critical electric field strength of ~ 8 MV/cm, enabling promising applications in next generation high power electronics and deep ultraviolet optoelectronics. The advantages of Ga_2O_3 also stem from its availability of single crystal bulk native substrates synthesized from melt, and its well-controllable n-type doping from both bulk growth and thin film epitaxy. Among several thin film growth methods, metalorganic chemical vapor deposition (MOCVD) has been demonstrated as an enabling technology for developing high quality epitaxy of Ga_2O_3 thin films, $(Al_xGa_{1-x})_2O_3$ alloys, and heterostructures along various crystal orientations and with different phases. This tutorial summarizes the recent progresses in epitaxial growth of β-Ga_2O_3 thin films via different growth methods, with a focus on the growth of Ga_2O_3 and its compositional alloys by MOCVD. The challenges for the epitaxial development of β-Ga_2O_3 are discussed, along with the opportunities of future works to enhance the state-of-the-art device performance based on this emerging UWBG semiconductor material system.

Keywords: Ultrawide bandgap, metalorganic chemical vapor deposition, Ga_2O_3, $(Al_xGa_{1-x})_2O_3$

I. Introduction on UWBG Ga_2O_3

Gallium oxide (Ga_2O_3), possessing a bandgap energy of ~ 4.5-5.3 eV [1-5], is a transparent semiconducting oxide material with excellent electrical and optical properties. Among the five different known polymorphs of Ga_2O_3 (α, β, γ, δ, and κ) as schematically illustrated in Figure 1, the monoclinic β-Ga_2O_3 (gallia) is the most thermally stable phase with a bandgap energy of ~ 4.8 eV [3, 6-9]. Its ultra-wide bandgap (UWBG) energy, ranging in the deep ultraviolet (DUV) spectrum,

allows its application in DUV optoelectronics, such as solar blind photodetectors. Recent demonstrations of β-Ga_2O_3 based diodes and transistors [10-12], on the other hand, have revealed the immense potential of this material in power switching applications due to its large critical field strength as compared to other wide bandgap (WBG) semiconductors such as GaN or SiC. In addition to its ultra-wide bandgap energy, the controllable doping of β-Ga_2O_3 as well as its availability of single crystal bulk native substrates promise its application in high power switching and radio-frequency (RF) electronics [13, 14].

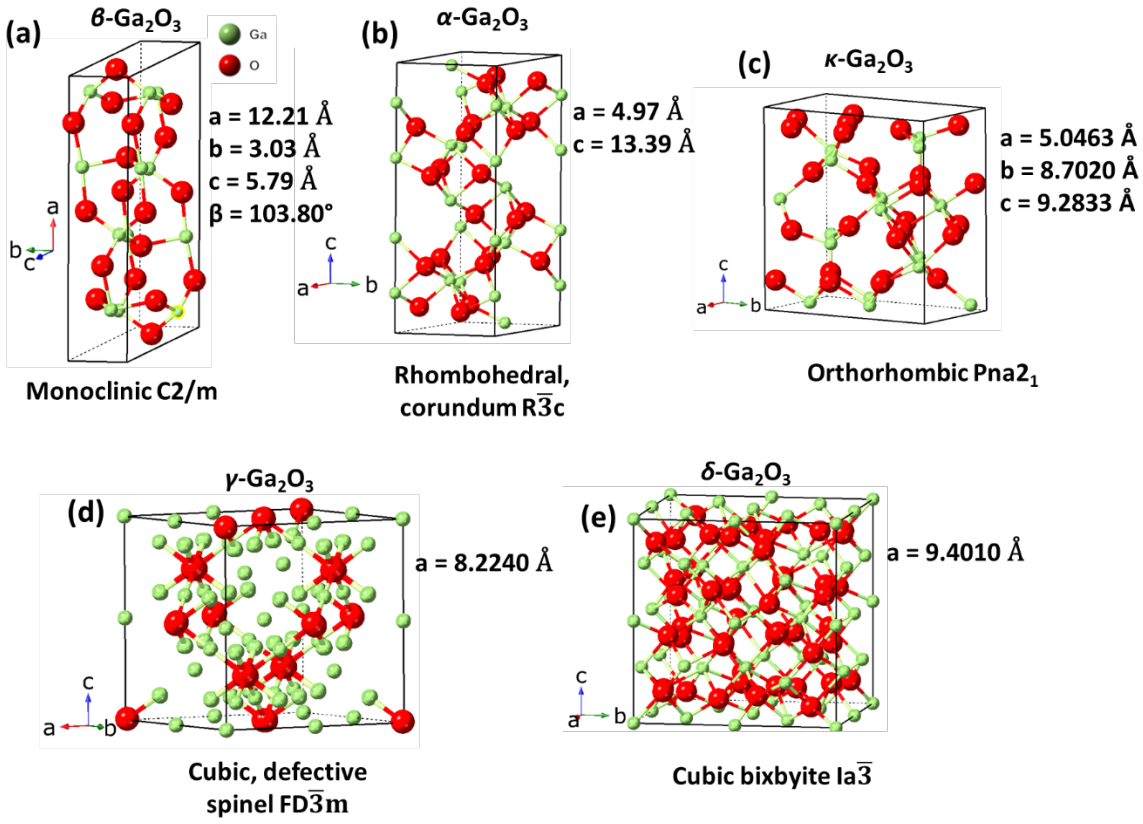

Figure 1. Crystal structure of (a) β-, (b) α-, (c) κ, (d) γ- and (e) δ-Ga_2O_3.

Density functional theory (DFT) calculations predicted the bandgap energy of β-Ga_2O_3 ranging between 4.5~4.9 eV [3, 8, 9, 15]. The critical field strength of β-Ga_2O_3 is projected at 7-8 MV/cm [10, 16, 18], which is 2.5-3.5 times higher than that of SiC (2.5 MV/cm), and GaN (3.3 MV/cm) [10, 17], indicating superior voltage blocking capabilities. Thus far, the highest peak electric field ~ 6 MV/cm has been experimentally demonstrated in β-Ga_2O_3 Schottky barrier diodes (SBDs) [18, 19].

The peak electric field in β-Ga_2O_3 is expected to improve with the further development of bulk β-Ga_2O_3 growth, thin film epitaxy and advanced device design/field management.

Unlike most other oxide materials with complex electron band structures, β-Ga_2O_3 conduction band structure is primarily contributed by the Ga s orbitals which is similar to the ones observed in GaN and GaAs [20]. The electron effective mass m_c^* for β-Ga_2O_3 is found to be light at 0.23 m_0 (m_0 is the free electron mass) [8, 9], similar to that of GaN and GaAs [21, 22]. Consequently, one would expect similar high electron Hall mobilities from Ga_2O_3 in the range of ~ 10^3 $cm^2/V.s$. However, the scattering effect from polar optical phonons (POP) was found to be more significant in Ga_2O_3 due to its asymmetric lattice structures and optical phonon modes [23-25], limiting its room temperature (RT) mobility to ~200 - 250 $cm^2/V.s$ [20, 24].

Despite its relatively low electron mobility at room temperature, β-Ga_2O_3 is predicted to outperform the traditional WBG semiconductors in power switching applications. For example, the Baliga's figure-of-merit (BFOM = $\varepsilon \cdot \mu \cdot E_c^3$) [26] of β-Ga_2O_3 (~ 3214, relative to Si) is 4X and 10X of GaN (~ 846) and SiC (~ 317) [10], indicating the potentially much lower conduction losses from β-Ga_2O_3 power devices. In terms of Johnson figure-of-merit (JFOM = $E_c^2 \cdot v_s^2/4\pi^2$) [27], which defines the power-frequency product of a transistor, Ga_2O_3 also exhibits higher JFOM of ~ 2844, as compared to GaN (JFOM ~ 1089) and SiC (JFOM ~ 278) due to its high electron saturation velocity (v_s ~ 1.2–2.0×10^7 cm/s) as suggested by the theoretical calculations [23, 28]. The summary of the fundamental properties and figure-of-merits of β-Ga_2O_3 electronic devices as compared to Si and other wide and ultrawide bandgap semiconductors are listed in Table 1. The large critical field E_c is a key material parameter that determines the great potential of Ga_2O_3 in applications of both high power and radio frequency electronics with excellent figure-of-merits.

Table 1. Properties of β-Ga_2O_3 as compared to Si and other (U)WBG semiconductors [10, 14, 29-31] .

Material Parameters	Si	4H-SiC	GaN	β-Ga_2O_3	AlN	Diamond	cBN
Bandgap E_g (eV)	1.1	3.25	3.4	4.8~4.9	6.2	5.5	6.4
Critical Field E_C (MV/cm)	0.3	2.5	3.3	8	15.4	10	17.5
Dielectric constant ε	11.8	9.7	9	10	9.76	5.5	7.1
Electron mobility μ_e ($cm^2/V.s$)	1480	1000	1250	300	426	2000	825
Thermal Conductivity ($W \cdot m^{-1} \cdot K^{-1}$)	150	490	230	10-27	320	2000	2145
Saturation Velocity (10^7 $cm \cdot s^{-1}$)	1	2.0	2.5	1.8-2.0	1.3	1	--
Baliga's FOM ($\varepsilon \cdot \mu \cdot E_C^3$)	1	317	846	3214	38180	24660	79000
Johnson's FOM ($v_{sat}^2 E_C^2/4\pi^2$)	1	278	1089	2844	4453	1100	--
Doping	n, p	n, p	n, p	n	n, p-	n-, p	n-, p-

Applications of Ga_2O_3 for next generation high power devices have two key advantages. One is the controllable n-type doping, which has been demonstrated so far with primary dopants of Si, Ge, and Sn in a wide range from low-10^{16} cm^{-3} to high-10^{20} cm^{-3} [32-37]. This wide range of doping fulfills the requirements of, for example, the low doped, thick drift layers for high voltage blocking capabilities, as well as the highly doped n^+ layers for forming Ohmic contacts with low resistance. Another major advantage of Ga_2O_3 is the availability of high-quality, scalable bulk β-Ga_2O_3 substrates with low density of defects, which can be prepared by melt-grown methods such as Czochralski (Cz) method [38, 39], edge-defined film-fed growth (EFG) [40, 41], floating zone (FZ) method [42, 43], and vertical Bridgman (VB) methods [44, 45]. Thus far, β-Ga_2O_3 wafers with 6" diameter were demonstrated [46]. As the wafer size scales up and the technology is adopted by industries, it is anticipated that the cost of Ga_2O_3 wafers will reduce [47]. The Ga_2O_3 substrate technology is considered as a key advantage of this material among the existing UWBG semiconductor candidates.

While Ga_2O_3 stands out as a promising UWBG semiconductor material for next generation high power and high frequency electronic and optoelectronic applications, there exist certain limitations of the material that need to be addressed in order to fully maximize its potential. The lack of p-type conductivity could be a major setback for Ga_2O_3 device design. It is theoretically

calculated that all major acceptor candidates for β-Ga_2O_3 act as deep acceptors [48, 49], indicating a very low activation efficiency and a trap-like behavior of the acceptors. Additionally, it is also theoretically predicted that, the holes in many oxides (Ga_2O_3, In_2O_3, SnO_2, MgO) prefer the localized, self-trapped form of polarons around O-site due to the characteristic lattice distortion [50]. Even if there are activated holes, the conductivity of such holes will be extremely low, prohibiting the p-type conductivity in such materials. Therefore, it would require novel device designs and engineering approaches to overcome the lack of p-type conductivity. Designs such as fin-structured SBDs and FETs [51, 52], as well as using high-k dielectrics in SBDs [19], or heterojunctions of p-n diodes formation by adopting other p-type semiconductors (p-NiO, p-Ir_2O_3) [53-57], are good examples of such attempts to overcome the lack of p-type conductivity in Ga_2O_3.

Thermal conductivity is yet another challenge for Ga_2O_3 in power electronics applications. The thermal conductivity λ for β-Ga_2O_3 was measured with strong anisotropy from the highest $\lambda \sim 27$ W/mK along [010] direction to the lowest $\lambda \sim 10$ W/mK along [100] direction [58], which are significantly lower than those of the traditional semiconductors (Si ~ 150 W/mK, SiC ~ 490 W/mK, GaN ~ 230 W/mK) [14]. The low thermal conductivity of Ga_2O_3 creates self-heating effects that could impact device performance and reliability, suggesting the need for effective heat extraction design in Ga_2O_3 devices. Common strategies to reduce the thermal resistance include substrate thinning as well as the wafer-bonding process to the substrates with high thermal conductivity, such as Cu, SiC, or diamond [59-61].

With its unique properties, UWBG Ga_2O_3 has gained significant research interests, and publication numbers in recent years increased dramatically [14, 62]. In the past decade, the emergence of high-quality bulk substrates, development of epitaxial growth and the successful demonstration of Ga_2O_3-based devices well exemplify the superior properties and potential of Ga_2O_3. Significant efforts have led to the advancements in understanding defects, doping, impurities, alloys, heterostructures, electron transport and thermal properties in Ga_2O_3 [63-67].

The focus of this tutorial is to provide a comprehensive introduction to the metalorganic chemical vapor deposition (MOCVD), also known as metalorganic vapor phase epitaxy (MOVPE), of Ga_2O_3 thin films, as well as its alloys and heterostructures. The tutorial emphasizes the homoepitaxial growth of β-Ga_2O_3 and its alloys, primarily because of its availability of high quality and scalable native substrates grown from melt. This advantage is specific to Ga_2O_3, distinguishing

it from other UWBG semiconductors. The tutorial is structured as follows. Section II provides an overall background on the state-of-the-art Ga_2O_3 thin film deposition technologies. Section III discusses the current status of MOCVD Ga_2O_3 technology, including the MOCVD reactor setup, precursor chemistry, and growth mechanisms. Section IV primarily focuses on the MOCVD development of compositional $(Al_xGa_{1-x})_2O_3$ alloys and heterostructures. Section V presents on the application of MOCVD Ga_2O_3 thin films and its alloys for device development. Finally, the conclusions with future perspectives for MOCVD Ga_2O_3 are presented in Section VI.

II. Thin film epitaxy of Ga_2O_3

Prior to the introduction of MOCVD Ga_2O_3, an overview on Ga_2O_3 epitaxy by different growth techniques is summarized. Thin film epitaxy is one of the cornerstone processes for the fabrication of high-performance devices, which provides precise control of doping, film thickness and layer structures. The Ga_2O_3 thin film epitaxy has been developed fast in the past decade with the most common growth techniques, including MOCVD, halide vapor phase epitaxy (HVPE), molecular beam epitaxy (MBE), mist chemical vapor deposition (Mist-CVD), low pressure chemical vapor deposition (LPCVD), pulsed laser deposition (PLD) and atomic layer deposition (ALD). A summary of the physical properties and the epitaxial growth methods utilized to grow the five different crystal phases of Ga_2O_3 is presented in Table 2. These technologies with different growth chemistries have their own pros and cons when targeting for different device designs and applications. In this section, a brief description of each growth method is presented. The content on MOCVD technology is included in Section III.

Table 2. Summary of the physical properties and the epitaxial growth methods utilized to grow the five different crystal phases of Ga_2O_3 [4, 14, 68-75].

	α	***β***	***γ***	***δ***	***κ***
Crystal structure	Corundum	Monoclinic	Cubic defective spinel	Cubic bixbyite	Orthorhombic
Lattice parameters (Å)	a = b = 4.98-5.04, c = 13.43-13.62	a = 12.12-12.34, b = 3.03 and 3.04, c = 5.80-5.87	a = 8.24-8.30	a = 9.4-10	a = 5.0463 b = 8.7020 c = 9.2833
Space group	$R\bar{3}c$	C2/m	$FD\bar{3}m$	$Ia\bar{3}$	$Pna2_1$
Bandgap (eV)	5.2- 5.41	4.5-4.9	4.5-5.0	4.8-5.0	4.6-4.9
Refractive index (n)	1.74-1.95	1.68-1.89	2.0-2.1	1.8	-
Thermal conductivity (W cm^{-1} K)	-	0.27 (010), 0.11 (100)	-	-	-
Polarization (μC cm^{-2})	-	-	-	-	26
Epitaxial growth methods	Mist CVD, MOCVD, HVPE, ALD	MBE, MOCVD, mist CVD PLD, HVPE, LPCVD sputtering, ALD	mist CVD	mist CVD	PLD, mist CVD, HVPE, MOCVD, ALD, MBE
References	**75-82**	**36, 37, 81, 83-100**	**101**	**74**	**70, 71, 102-112**

II.a HVPE

HVPE is a widely used method for growth of III-nitride and oxide semiconductors [92, 113, 114]. It utilizes the in-situ generated group-III metal chlorides at high temperature as precursors. In oxide HVPE, the metal chloride reacts with oxygen under atmospheric pressure at certain growth temperatures (typically ~ 1000 °C) to deposit thin films on substrates [33, 92, 113-115]. HVPE *β*-Ga_2O_3 offers high growth rates (~ 5 μm/hr, up to 250 μm/hr) [114, 115], allowing thick layer deposition, but typically with rough surface morphologies, which requires chemical mechanical polishing (CMP) process prior device fabrication. For n-type doping, Si is typically incorporated by the introduction of $SiCl_4$ gas, and the doping concentration ranges from 10^{15}-10^{19} cm^{-3} [34]. High-quality HVPE *β*-Ga_2O_3 thin films have been demonstrated with RT carrier mobility around 150 cm^2/V.s and low carrier concentration around 10^{15} cm^{-3} [33]. Other crystal phases (*α* and κ) of Ga_2O_3 were also

demonstrated by HVPE heteroepitaxy on different substrates at a much lower growth temperature (500-900 °C) [107, 116].

II.b MBE

MBE is one of the early growth techniques used for Ga_2O_3 epitaxy. Different from growth methods that transport the precursors in the gas phase, MBE utilizes ultra-high vacuum (~10^{-12} Torr) and effusion cells to sublime the metal sources. Under high-vacuum conditions, the mean free path for molecules becomes long enough that the precursors are ballistically transported to the substrate like a beam. In MBE Ga_2O_3, there are generally two types of oxidation source: oxygen plasma [117] and ozone [87], and the typical growth temperature ranges between 500 - 800 °C [36, 88, 90, 117, 118]. The growth rate of MBE Ga_2O_3 is relatively slow (around 50-200 nm/h) [88, 117, 118], which also enables precise control over thin layer epitaxy, such as Ga_2O_3 Si delta-doped layer [119, 120]. The implementation of indium (In) flux during MBE of β-Ga_2O_3 (metal-oxide catalyzed epitaxy, MOCATAXY) greatly reduces the surface desorption, resulting in the increase of growth rate and expansion of the growth regime to higher MBE growth temperatures on crystal orientations such as (001) and $(\bar{2}01)$ [121, 122]. In addition, the utilization of suboxide molecular-beam epitaxy (S-MBE) resulted in a remarkable improvement in the growth rates of Ga_2O_3 with excellent crystallinity, exceeding 1 μm/hr in an adsorption-controlled regime [123]. Heterostructures of $(Al_xGa_{1-x})_2O_3/Ga_2O_3$ have been demonstrated by MBE growth. The formation of 2-dimensional electron gas (2DEG) by modulation doping in β-$(Al_xGa_{1-x})_2O_3/Ga_2O_3$ heterostructure results in much lower sheet resistivity and promising carrier transport properties [124, 125].

II.c Mist-CVD

Mist-CVD growth technique is considered as a low cost and simple approach which is efficient in reducing the oxygen vacancies as the growth is performed under sufficient overpressure of oxygen using water/alcohol solutions. For the growth of Ga_2O_3 thin films, gallium acetylacetonate $[Ga(C_5H_8O_2)_3]$ in water is ultrasonically atomized to create a mist which is carried to the heated substrate by using O_2 or N_2 carrier gas to form thin films by chemical reaction. Different polymorphs of Ga_2O_3 including α-, β-, and ε- have been grown by using this growth technique [57, 82, 93, 109, 126-128]. Heteroepitaxial growth of α-Ga_2O_3 thin films on c-plane sapphire substrates [82, 126-128] and homoepitaxial growth of β-Ga_2O_3 films on (010) oriented β-Ga_2O_3

substrates have been demonstrated [93]. While controllable n-type doping in a range of 10^{17} to 10^{19} cm^{-3} was achieved in α-Ga_2O_3 heteroepitaxial films grown on c-plane sapphire substrates using Sn as dopant, the mobility was found to be limited (< 24 cm^2/Vs) due to the crystal defects such as dislocations in the epi-layer [128]. Since α-Ga_2O_3 is metastable, the growth window for the phase pure α-Ga_2O_3 remains narrow as compared to β-Ga_2O_3. High temperature growth (> 550°C) on sapphire substrates leads to inclusion of β-phase. On the other hand, electrically conductive Sn-doped β-Ga_2O_3 homoepitaxial films were grown on Fe-doped β-Ga_2O_3 substrates at a growth temperature of 700°C with a carrier concentration of 10^{18} cm^{-3} and hall mobility of 45 cm^2/Vs [93].

II.d LPCVD

In LPCVD growth of Ga_2O_3, high purity metallic Ga and O_2 are used as sources, and $SiCl_4$ is used as n-type dopant. Growths are performed in the temperature range between 750°C to 1050°C [34, 94, 95, 129-133]. By tuning the growth conditions (growth temperature, precursor flow, pressure, etc.), the growth rate can be controlled between ~ 1 - 10 μm/hr [34, 131, 132]. Both unintentionally and Si-doped high-quality LPCVD homoepitaxial β-Ga_2O_3 thin film growths on (010) and (001) β-Ga_2O_3 substrates have been successfully demonstrated [131]. For heteroepitaxy, we have demonstrated the use of off-axis c-sapphire substrates to overcome the issue caused by lattice-mismatch. Room temperature mobility for β-Ga_2O_3 grown on off-axis c-sapphire exceeded 100 $cm^2/V{\cdot}s$, which represents one of the record value for β-Ga_2O_3 heteroepitaxy [34]. LPCVD growth technique represents a low cost and scalable growth method that can potentially produce high-quality and thick drift layers for vertical SBDs [134]. In addition, LPCVD growth technique has also been demonstrated to grow high-quality In_2O_3 films with fast growth rates [133, 135].

II.e PLD

PLD is a simple and versatile deposition method that is effective in depositing doped thin films and heterostructures at relatively low deposition temperature. In PLD, the target material is physically vaporized by pulsed laser and consequently deposited on the substrates. However, the low operating temperature also leads to the lower material quality, as well as the low deposition rate. PLD is a common technique for depositing transparent conducting oxide. It has been demonstrated as a feasible technology for the deposition of highly n-type doped conductive β-

Ga_2O_3 films [35]. The typical growth temperature for PLD ranges from 500 to 800 °C [35, 136, 137]. In addition to β-phase Ga_2O_3 deposition, PLD of κ-Ga_2O_3 on sapphire substrates was reported [111, 138].

II.f ALD

ALD or atomic layer epitaxy (ALE) is a growth technique with sequential gas injection, and self-limiting reaction characteristics. The precursors are injected by pulses into the chamber and each pulse has its own limited surface reactions for a very thin layer (atomic layer) of deposition. The ALD method operates under low deposition temperature with relatively lower growth rate. However, due to the pulsing injection of precursors, growth rate by ALD can be precisely controlled [139]. Depending on the selection of precursor and temperature, amorphous oxides can be deposited with high surface uniformity, which makes ALD a widely used technique for dielectric deposition [81, 140, 141].

III. Overview on MOCVD β-Ga_2O_3

MOCVD growth of β-Ga_2O_3 has been demonstrated with high crystalline quality and effective n-type doping. Triethylgallium (TEGa), Trimethylgallium (TMGa), $Ga(DPM)_3$ (DPM = dipivaloylmethanate), high purity O_2, H_2O vapor, or N_2O have been used as precursors [32, 37, 83, 100, 142-146]. Si, Sn, and Ge were demonstrated as effective shallow donors [32, 83, 144]. Tetraethylorthosilicate (TEOS) and silane (SiH_4) have been used as Si source, whereas tetraethyltin (TESn) and Germane (GeH_4/N_2) were used as Sn and Ge sources, respectively. Previously, IKZ (Germany) demonstrated homoepitaxial growth of β-Ga_2O_3 on (010) native substrates with mobility up to 130 $cm^2/V{\cdot}s$, with Si doping concentration between 1×10^{17} to 8×10^{19} cm^{-3} [32]. However, using Sn as a dopant, the doping range was limited to 4×10^{17} - 1×10^{19} cm^{-3} with mobilities ranging between ~50 -100 $cm^2/V{\cdot}s$ [32]. This limitation was attributed to the Sn memory effect in the MOVPE reactor, indicating challenges to achieve low carrier densities and incorporation issues that decreased the doping efficiency at high Sn doping levels. Additionally, a recent study on Ge doping of Ga_2O_3 by MOCVD also revealed challenges in achieving controllable Ge doping for n-type conductivity [144]. A free carrier concentration ranging from $\sim 2 \times 10^{16}$ to $\sim 3 \times 10^{20}$ cm^{-3} with corresponding mobilities ranging from ~140 to ~38 $cm^{2/}Vs$ were achieved. The study showed that lowering the growth temperature increased Ge doping concentration, and the incorporation of Ge into the films was dependent on the metalorganic precursor type. Doping

Ga_2O_3 with Ge was found to be more difficult when using TMGa as a Ga precursor, compared to using TEGa. The study also revealed a strong memory effect of Ge doping dependent on the reactor geometry. Using a vertical far-injection reaction chamber, high-quality UID Ga_2O_3 homoepitaxy with room temperature mobility of 176 $cm^2/V{\cdot}s$ with background concentration of 7×10^{15} cm^{-3} was demonstrated [37]. Recent demonstration of lightly-doped (010) Ga_2O_3 exhibited low temperature peak mobility of > 10^4 $cm^2/V{\cdot}s$ from low-temperature Hall measurement (45K) [147], indicating ultra-high purity of MOCVD grown Ga_2O_3. A close-coupled showerhead design to overcome the limited growth rate in MOCVD Ga_2O_3 systems has also been demonstrated. By reducing the distance between the showerhead and substrate susceptors, the gas-phase reaction between MO sources and oxygen could be suppressed, leading to a fast growth rate of 10 μm/hr on sapphire substrates [145]. While TMGa shows promises for achieving faster growth rates, the homoepitaxial growth of Ga_2O_3 films using TEGa faces challenges as the film thickness increases, limiting the development of thicker drift layer for vertical power devices. Thus far, the typical growth rate for high-quality homoepitaxial Ga_2O_3 using TEGa as Ga precursor is in the range of ~ 1μm/hr [83, 84]. Another key contribution of the MOCVD growth technique is the demonstration of high-quality β-$(Al_xGa_{1-x})_2O_3$ epitaxy with high Al incorporation up to 40% on native (010) substrates [148]. These results indicate a great potential of MOCVD growth method for developing high-quality β-Ga_2O_3 based thin films and heterostructures for high-performance device applications.

A comprehensive investigation of the bandgap states in MOCVD-grown β-Ga_2O_3 utilizing Deep-Level Transient Spectroscopy (DLTS), Deep Level Optical Spectroscopy (DLOS), and admittance spectroscopy (AS) revealed a significant decrease (~10x reduction) in the overall trap concentration as compared to the prior studies on the full bandgap spectrum of defects in the films grown by PAMBE and EFG [149]. By systematically studying the deep level defect evolution as a function of MOCVD growth temperature, a distinct concentration trends for various bandgap states were observed [150]. A noteworthy observation was the increasing prevalence of the E_C-0.12 eV state, which seems to be associated with Si concentration, and the simultaneous decrease of the E_C-4.4 eV state concentration as the growth temperature rises from 800 °C to 920 °C, suggesting strong influence of MOCVD growth conditions on the distribution (concentrations and energy levels) of individual defect states of Si-doped β-Ga_2O_3. The growth temperature also plays a crucial role in adatom diffusion at the growth surface, which in turn strongly influences the surface morphology

of β-Ga_2O_3 [83]. Lower growth temperatures (~800 °C) resulted in a rougher surface with visible macroscopic dents, whereas a uniform and smooth surface was observed at 880 °C [83]. Another study on MOCVD homoepitaxial growth of β-Ga_2O_3 films revealed decent transport characteristics with atomically flat surfaces at growth temperature below 700 °C [151], indicating a wider MOCVD growth window in terms temperature. The use of low temperature (600 °C) buffer layer also enhanced the Hall electron mobility of unintentionally doped as well as Si-doped β-Ga_2O_3 films [152]. A monotonous decrease in the film growth rate was observed with the increase of chamber pressure from 20 to 100 Torr [83], resulting in higher Si incorporation in the film. This was likely caused by a reduction in precursor diffusion from the gas phase to the growth surface and an increase in the gas-phase reaction of the precursors.

In addition to β-Ga_2O_3 MOCVD growth on (010) Ga_2O_3 substrates, (100) Ga_2O_3 epitaxy attracted quite significant interests. While on-axis growth of (100) β-Ga_2O_3 leads to incoherent boundaries, stacking faults, and degraded carrier transport, the vicinal (100) substrates with off-axis angles between 2° to 6° were selected to address these issues by suppressing twinning domains. These studies provide important insights into surface and chemical reaction kinetics of MOCVD Ga_2O_3 growth on (100) orientation [99, 153, 154].

Another major challenge for high-quality MOCVD β-Ga_2O_3 epitaxy is the gas-phase reaction of precursors above the growth surface. The typical growth rate ranges from 0.2~1.0 μm/h, primarily limited by the gas phase reaction, in which TEGa was predominantly used as the precursor for Ga_2O_3 epitaxy. However, until recently, it has been demonstrated that TMGa source could deliver high-quality homoepitaxy (growth rate < 3 μm/hr) as comparable to the ones grown by TEGa [142, 146]. In Fig. 2, the state-of-the-art MOCVD growths, using different precursors, dopants, growth conditions and substrates, are shown in RT electron Hall mobilities as a function of net charge concentration.

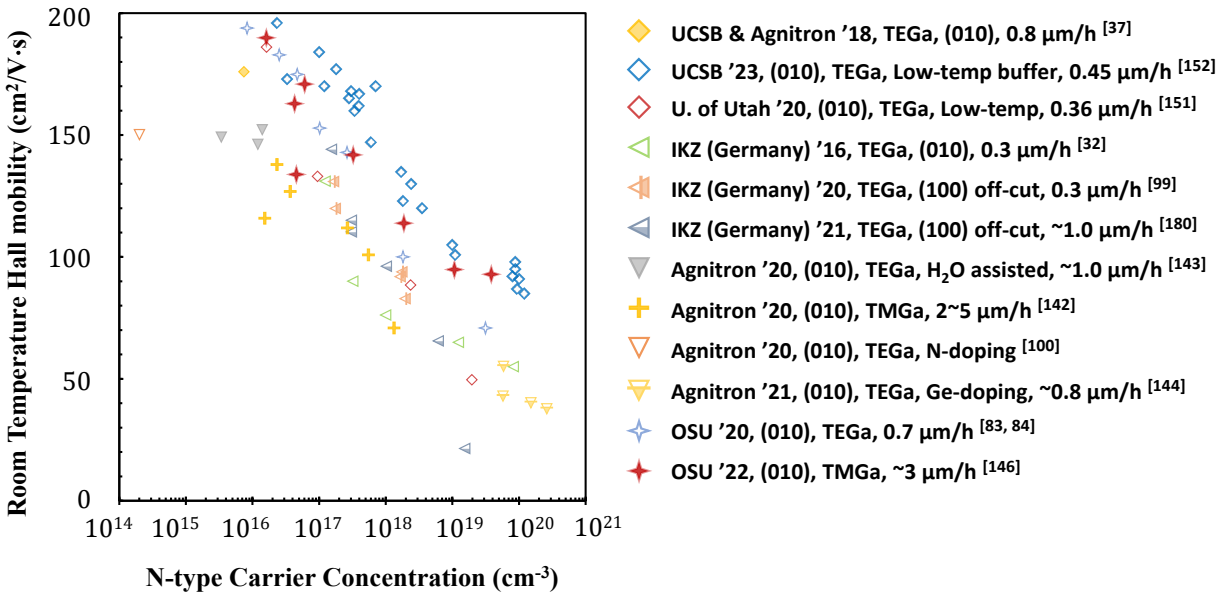

Figure 2. Room-temperature mobility versus net carrier concentration from the state-of-the-art β-Ga_2O_3 thin films grown by MOCVD. The corresponding growth rates are also listed.

While MOCVD homoepitaxial growth of β-Ga_2O_3 thin films showed superior structural and electrical characteristics, recently few research was also devoted to the heteroepitaxial growth of β-Ga_2O_3 films [155-159] and its alloys [160, 161] on different substrates, including c-sapphire, GaAs and Si. However, MOCVD β-Ga_2O_3 epilayers grown on these foreign substrates did not exhibit satisfactory structural and electrical properties. When using on-axis c-plane sapphire as a substrate for heteroepitaxy, β-Ga_2O_3 grows with its $(\bar{2}01)$ orientation aligned to the sapphire (0001) plane with rotational domains and lattice distortions [162]. The growth of $(\bar{2}01)$ β-Ga_2O_3 was also observed on GaAs substrates of varying orientations [155]. A prior MOCVD growth study revealed amorphous Ga_2O_3 films on Si substrates [158], indicating that the selection of substrate plays a significant role in the crystalline structure and quality of Ga_2O_3 epifilms.

III.a Chemical reaction kinetics in MOCVD Ga_2O_3

The schematic in Fig. 3 shows the typical oxide MOCVD system. Major components in MOCVD system include gas/precursor delivery system, source injection control, showerhead, the main reactor chamber with RF heating coil and pressure controlling units with high-capacity pump.

The design considerations for a MOCVD reactor are unique compared to other types of CVD techniques that operate at atmospheric or low pressure, ultra-high vacuum, or plasma-enhanced conditions [163-166]. This includes the handling of volatile precursors, delivery of uniform, consistent gas flow to the substrates, precision control of the reactor pressure, effective heating and cooling of the reactor component to reach the desired temperature gradient, fast switching valves to switch sources for precise multilayer growths.

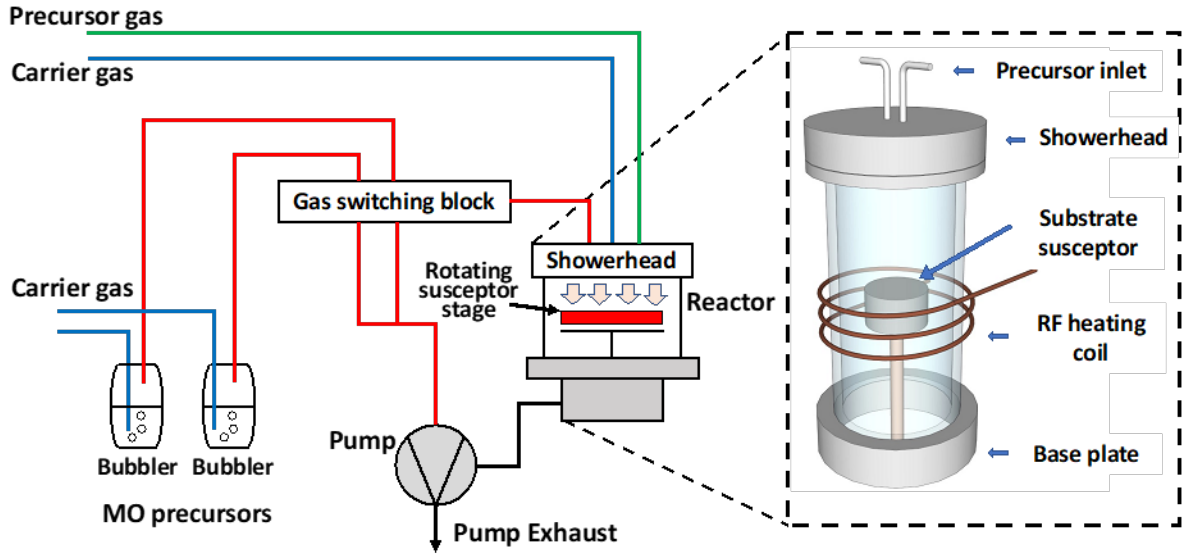

Figure. 3: Schematic of a typical oxide MOCVD system.

For precise control of multiple layer growths via MOCVD, the gas switching needs to be executed in a timely manner and reflected immediately with source altered on growth surface. The precursor delivery system is typically made of an array of high-purity MO precursors held in individual bubblers, with each source having its own settings of bubbler temperature, carrier gas flow and pressure. The source injection control is controlled by a critical component, usually named injection block. Showerhead is the gas block that regulates the source gases fed from pipelines into stable, homogenous flow to ensure that the source is uniformly delivered to the growth surface, where the geometry of the reactor chamber and typical chamber pressure need to be considered. With appropriate designs, MOCVD epitaxy could achieve high-quality, uniform thin films on large wafers. In some designs, the substrates are placed on a fast-rotating susceptor to further enhance the uniformity of the growth.

Previously, the growth mechanisms of MOCVD oxides were primarily focused on ZnO and perovskite oxides. For MOCVD III-oxides (Ga_2O_3, Al_2O_3, In_2O_3) and compositional alloys, the studies on chemical reactions are still limited. Due to the reactive nature of the metalorganic sources, triethylgallium was primarily chosen as the precursor for Ga_2O_3 epitaxy, and the growth rate is potentially limited by the gas-phase reaction between MO precursors and oxidation source. However, the general reaction/deposition process in MOCVD, as shown in Fig. 4, consists of several key steps: 1) Transport of the precursors to reactor region in the form of vapors. 2) Gas-phase pre-reactions of precursors, these also include pyrolysis and adduct formation of the chemical species. 3) Mass transport of the chemical active species to substrate surface. 4) Adsorption of the reactants to the substrate surface. 5) Surface diffusion of adatoms to the growth sites, nucleation, and surface chemical reactions, leading to the thin film deposition. 6) Desorption and mass transport of precursor fragments from substrate surface [154, 167, 168].

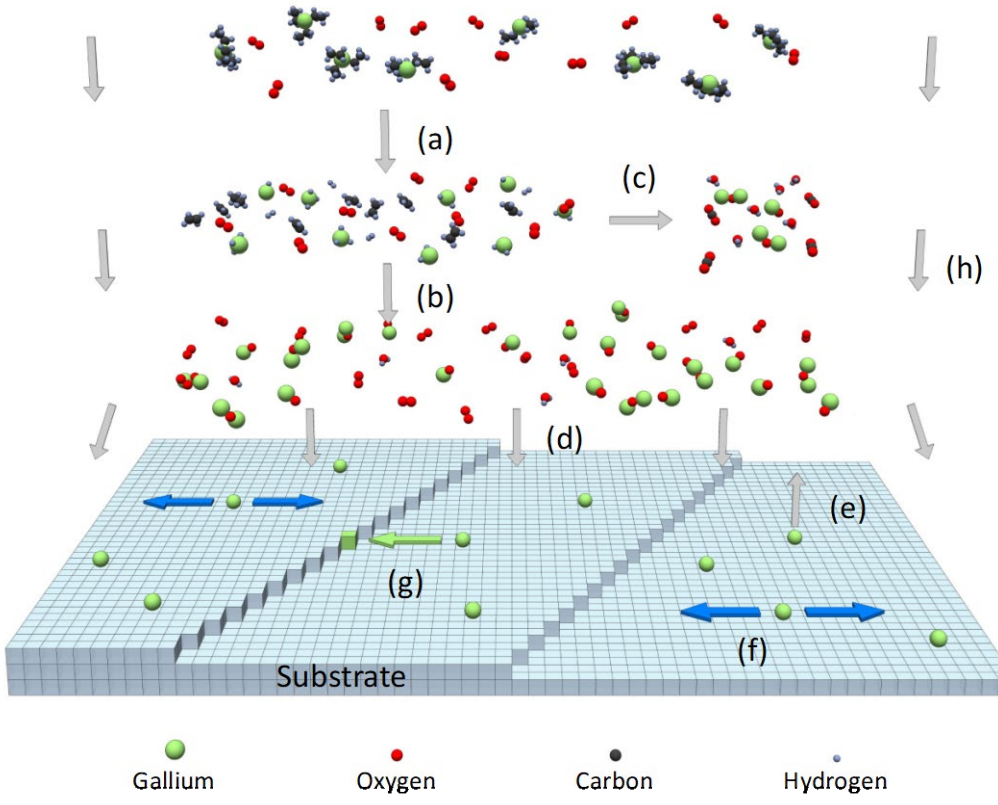

Figure 4. Schematic of typical processes occurring in MOCVD Ga_2O_3 reactor using TEGa and O_2 as precursors: (a) precursor breakdown, (b) precursor prereactions, (c) byproduct formation, (d)

surface adsorption of adatoms, (e) surface desorption of adatoms, (f) surface diffusion of adatoms, (g) incorporation of adatoms at incorporation sites, and (h) gas transport by the carrier gas.

Among these steps, different physiochemical kinetics are involved. The dominant kinetics, that determine the growth characteristics such as reaction rate, deposition rate, uniformity, and impurity incorporation, are highly dependent on the growth parameters such as temperature, pressure, gas flow, and concentrations of chemicals. For instance, one of the key factors that determine the deposition rate is the growth temperature. It is commonly categorized into three temperature regions. At lower growth temperatures, the deposition rate is primarily controlled by chemical reaction kinetics. The growth rate corresponds to the surface reaction rate of the chemical compounds, which increases exponentially with substrate temperature according to the Arrhenius law. As growth temperature increases, the deposition rate is primarily limited by the amount of chemical species reaching the growth surface by mass transport or diffusion of chemical species. As growth temperature becomes excessively high, the growth rate may decrease due to the depletion of precursors in the gas-phase, as the boundary layer near substrates gets enough heated and promotes significant pre-reaction of precursors. Additionally, the surface desorption and decomposition process can also be significantly promoted, leading to lower growth rates.

One key trait for oxide MOCVD is the pyrophoricity of the MO sources. The reactivity of the MOCVD precursors is mostly determined by the nature of organic moiety attached and the electropositive metallic character [169]. Typically, higher reactivity with less stability is associated with higher metal-carbon bond energies [169]. Similar to this, a key factor in the reactivity of metalorganics is the stability of the resultant alkyl radical as well as the reduction in metal-carbon bond strength caused by increased steric bulk and branching in the alkyl radical [170]. During MOCVD growth of Ga_2O_3, the incorporation of carbon into the growing layer poses a significant challenge as it originates from metalorganic precursors. While TMGa and TEGa are commonly used as precursors for Ga_2O_3 epitaxy, one main concern of using TMGa is the high level of carbon incorporation into the growing layers due to the formation of highly reactive methyl radicals during the pyrolysis process as discussed in later paragraphs. On the other hand, TEGa produces a stable ethylene group, which has limited participation in substrate surface reactions, thus effectively reducing carbon incorporation into the growing layer. This makes TEGa a potentially preferable option over TMGa for achieving lower levels of carbon incorporation in Ga_2O_3 films [171, 172].

With few research on the growth dynamics and chemical kinetics, MOCVD growth of semiconducting β-Ga_2O_3 has recently been explored. In the most recent work by Goto et al., the thermodynamics of MOCVD β-Ga_2O_3 using triethylgallium (TEGa) and oxygen was analyzed [173]. The metal alkyl precursors are known for their pyrophoric property. The electropositive character of the metal elements such as Al, Ga, In, and Zn, as well as the moiety of organic ligands (methyl, ethyl) lead to strong reactivity with oxygen or moisture. The reaction models for MOCVD Ga_2O_3 is, therefore, vastly different from the models for III-V or III-nitrides. The major reactions involving the decomposition pathways of TEGa (Eq. (1)- Eq. (4)) and TMGa (Eq. (5)- Eq. (7)) precursors and oxidation reactions are listed below. TEGa is pyrolyzed through a three step β-hydride elimination reaction with formation of gallium hydride and ethylene as by-products [171, 174, 175].

$$Ga(C_2H_5)_3 \rightarrow HGa(C_2H_5)_2 + C_2H_4 \qquad \text{Eq. (1)}$$

$$Ga(C_2H_5)_2 \rightarrow H_2Ga(C_2H_5) + C_2H_4 \qquad \text{Eq. (2)}$$

$$Ga(C_2H_5) \rightarrow GaH_3 + C_2H_4 \qquad \text{Eq. (3)}$$

The expected reaction of gallium hydride with O_2, in order to form Ga_2O_3, can be as follows.

$$2GaH_3 + 3O_2 \rightarrow Ga_2O_3 + 3H_2O \qquad \text{Eq. (4)}$$

TMGa, on the other hand, undergoes a two-step unimolecular reaction with the loss of methyl groups, resulting in the formation of monomethylgallium.

$$Ga(CH_3)_3 \rightarrow Ga(CH_3)_2 + CH_3 \qquad \text{Eq. (5)}$$

$$Ga(CH_3)_2 \rightarrow Ga(CH_3) + CH_3 \qquad \text{Eq. (6)}$$

While there are still lack of studies on the reaction mechanism between TMGa subproducts and O_2 to form Ga_2O_3, we can hypothesize that monomethylgallium reacts with O_2 to form Ga_2O_3 through the following reaction.

$$2Ga(CH_3) + 3O_2 \rightarrow Ga_2O_3 + 3H_2O + 2CO_2 \qquad \text{Eq. (7)}$$

The hydrogen and hydrocarbon by-products are consumed via combustion processes and turn into CO, CO_2 and H_2O. The reaction pathway for hydrocarbons indicates that it is less likely to

contribute in carbon incorporation in MOCVD β-Ga_2O_3 as compared to MOCVD III-V and III-nitrides. Kinetic calculations also suggest that higher growth temperature and higher VI/III ratio could further suppress the incorporation of carbon. Most importantly, the gas phase reactions between precursors and O_2 are very active. It is therefore inferred that the mass transport of Ga species to the growth surface is one of the key limiting factors for MOCVD β-Ga_2O_3 growth. Hence, suppression of the gas phase reactions can enhance the deposition rate of β-Ga_2O_3. Since TMGa decomposes through a two-step reaction, while TEGa follows a three-step pyrolysis process, the shorter reaction pathway in TMGa leads to higher growth rates of Ga_2O_3 films compared to the processes utilizing TEGa. MOCVD β-Ga_2O_3 growth rates typically range from 0.2 to 1.0 μm/h when TEGa is used as the Ga precursor. In contrast, β-Ga_2O_3 films grown using TMGa as the Ga precursor has been demonstrated with faster growth rates up to 3 μm/h with decent transport characteristics comparable to the films grown using TEGa [142, 146].

III.b MOCVD β-Ga_2O_3 homoepitaxy on different crystal orientations

Considering the low symmetry of the monoclinic crystal structure, epitaxial growth of β-Ga_2O_3 was primarily established on (010) orientation with high quality and excellent electronic transport characteristics [83, 84]. One exception could be the homoepitaxy by HVPE, which was demonstrated along the [001] orientation [33]. However, this technique results in relatively rough surface morphologies that require chemo-mechanical polishing (CMP) prior device fabrication. Several limiting factors have proven the difficulties for epitaxial growth along different crystal orientations such as (100), (001), and $(\bar{2}01)$, which were made available in bulk substrates. These limiting factors include the limited growth rate, strongly faceted surface, three-dimensional surface structures, or crystal structure-related defects. Despite the extensive growth studies on (010) oriented Ga_2O_3 substrates, there is still a lack of MOCVD homoepitaxial development of β-Ga_2O_3 films on other orientations. In recent years, MOCVD growth studies on (100) Ga_2O_3 substrates, particularly on off-axis (100) substrates have been performed. Homoepitaxial growth on on-axis (100) Ga_2O_3 substrates leads to the formation of incoherent boundaries and stacking faults due to the limited diffusion length of the surface adatoms and 2D-island growth mode [154]. Therefore, the epilayer on (100) suffered from charge compensation and degradation of carrier transport [99, 153]. Vicinal (100) substrates with an off-axis angle between 2° to 6° were selected to address this issue.

The step edges on the growth surface provide additional nucleation sites, and thus enhance the step-flow growth mode, suppressing the formation of twinning.

The growth surface morphology of β-Ga_2O_3 can be described by the surface kinetics model, formalized by Bales et al. [176]. The model explains the nucleation and growth of islands on growth surface by assuming that the incoming adatoms are either incorporated into step edges or form two-dimensional islands. Prior studies on homoepitaxial growth of (100) β-Ga_2O_3 have suggested that the prevailing growth mode is the 2-D island formation mode. By introducing proper miscut angles on the substrates, step-flow growth of β-Ga_2O_3 on (100) plane can be achieved as the terrace width becomes comparable to the diffusion length of adatoms on the growth surface [154]. The limited surface diffusion of the Ga adatoms on growth surface results in the formation of twin lamellae, hampering the mobility of charge carriers. Prior studies indicated that the surface diffusion coefficient on the (100) β-Ga_2O_3 plane is approximately two orders of magnitude lower than that experimentally found in GaAs, yet it is six orders of magnitude higher than the reported values for cubic GaN [154]. The surface diffusivity is most likely to be dependent on the surface arrangement as well as the surface energy of the crystal planes. Epitaxial growth on (100) substrates with a miscut towards $[00\bar{1}]$ results in high-quality β-Ga_2O_3 films with good electrical transport properties [153, 177]. When the (100) plane is miscut oriented towards $[00\bar{1}]$ direction, the terraces on (100) plane are terminated by $(\bar{2}01)$ plane causing mono-layer formation with uniform step height which promotes step-flow growth [178]. However, when grown on substrates with miscut towards [001], the layer completely twins with respect to the substrate, leading to stacking mismatch boundaries that hamper electrical transport. Miscut along [001] direction provides mixture of mono- and bilayers with different step heights which cause twinning and leads to formation of 2D islands. The epitaxial growth on substrates with miscut towards the $[00\bar{1}]$ direction often leads to the formation of $(\bar{2}01)$ facets at step edges. The $(\bar{2}01)$ facet has significantly lower surface energies as compared to the (001) surface. When the substrate miscut is towards [001], no symmetrical surface equivalent to the $(\bar{2}01)$ facet exists, and therefore, the (001) facet is expected to form, since all other considered surfaces have higher energies. Nonetheless, experimental observations reveal the nucleation of a twinned $(\bar{2}01)$ terminated nucleus on the (001)-B facets, leading to a twinned orientation at the step edge, thereby a significant reduction of

the surface energy. Results from these studies revealed a strong influence of both substrate miscut angles and directions on the structural and electrical properties of β-Ga_2O_3 epitaxial layers.

Recent study also indicated that the step-flow growth mode could be achieved with different miscut angles by adjusting the diffusion length of the adatoms using different growth conditions, such as the O_2/Ga ratio, Ar push gas flow, and chamber pressure [99]. Very recently, MOCVD growth of unintentionally doped < 3 μm thick β-Ga_2O_3 films have been demonstrated on (100) oriented off-axis β-Ga_2O_3 substrate with smooth surface morphology and good electrical transport properties by using height-adjustable showerhead to suppress the gas-phase pre-reactions [179, 180]. These studies have shown the feasibility of developing Ga_2O_3 homoepitaxy along various crystalline orientations.

III.c Other Ga_2O_3 polymorphs grown using MOCVD

Using different growth conditions (e.g., temperature, pressure), precursors (e.g., oxidation source), and substrate selection, various phases of Ga_2O_3 could be grown by MOCVD on different substrates, such as sapphire (a-, c-, m-, r-planes), MgO (cubic), and $MgAl_2O_4$ (cubic, spinel) [155, 181, 182]. The scientific community has shown great interest in metastable rhombohedral corundum structured α-Ga_2O_3 (space group $R\bar{3}C$) due to its large bandgap of 5.3-5.41 eV [75]. This is primarily because α-Ga_2O_3 thin films can be epitaxially grown on low-cost isostructural sapphire substrates and its electrical conductivity can be regulated [183, 184]. Despite numerous studies on the growth of α-Ga_2O_3 using various growth techniques such as mist-CVD, MBE, and HVPE, limited research has been conducted on the MOCVD development of phase pure α-Ga_2O_3 films. Previously, α-phase Ga_2O_3 has been demonstrated by MOCVD on m-, and r-plane sapphire substrates, using oxidation sources of N_2O and O_2 [155, 185]. MOCVD growth of phase pure α-Ga_2O_3 films and its Al-alloy have been successfully demonstrated on m-sapphire substrates for entire Al composition range [75]. For the meta-stable γ-Ga_2O_3, there is no report of pure γ-phase grown by MOCVD. However, phase segregation and existence of γ-phase were extensively observed in epitaxial thin films [186-188] grown by different methods including MOCVD [187, 188]. The orthorhombic κ-phase Ga_2O_3 represents another interesting polymorph of Ga_2O_3, which is predicted to have strong spontaneous electrical polarization and ferroelectric characteristics [189]. In recent years, researchers have carried out several investigations on the growth of κ-Ga_2O_3, with MOCVD proving to be a

valuable tool in demonstrating high-quality heteroepitaxial growth of the binary compound, as well as the growth of Si-doped electrically conductive κ-Ga_2O_3 thin films [105, 182, 190]. κ-phase has typically been shown to be grown at relatively lower growth temperatures (~500-600 °C) through MOCVD [70, 102, 191, 192].

IV. Overview on MOCVD β-$(Al_xGa_{1-x})_2O_3$ alloys

While Ga_2O_3 with its predicted large critical field strength is considered as a promising candidate for high power electronic applications, the bandgap engineering of Ga_2O_3 by alloying with Al_2O_3 can extend its applications in integrated power electronics and radio frequency electronics with even higher critical field strength due to the tunable bandgap of $(Al_xGa_{1-x})_2O_3$ alloy (~4.87 eV [β-Ga_2O_3] to 8.82 eV [α-Al_2O_3]) [69]. As the two parent compounds (Ga_2O_3 and Al_2O_3) of $(Al_xGa_{1-x})_2O_3$ alloy exist in different crystal structures, namely monoclinic β-Ga_2O_3 and corundum α-Al_2O_3, the epitaxial growth of high-quality phase pure β-$(Al_xGa_{1-x})_2O_3$ faces certain challenges. Nevertheless, recent progresses on the MOCVD growth of β-$(Al_xGa_{1-x})_2O_3$ epitaxy exhibited great promises for the control of uniformity, composition, and purity of the AlGaO epilayer. Several efforts have been made on the epitaxial growth of β-$(Al_xGa_{1-x})_2O_3$ alloys on differently oriented β-Ga_2O_3 substrates by using MOCVD growth technique [148, 187, 188, 193-200]. Prior efforts on the MBE growth of phase pure β-$(Al_xGa_{1-x})_2O_3$ films on (010) oriented β-Ga_2O_3 substrates exhibited phase segregation as the Al composition reaches above 20% [201]. By using MOCVD growth method, Al incorporations up to 40-43% have been demonstrated in (010) β-$(Al_xGa_{1-x})_2O_3$ thin films [148, 187, 188, 202]. High crystalline quality β-$(Al_xGa_{1-x})_2O_3$ films and β-$(Al_xGa_{1-x})_2O_3$/β-Ga_2O_3 superlattice (SL) structures with abrupt interfaces and uniform Al distribution were achieved up to Al compositions of ~27% [148]. However, due to the asymmetric bonding strength of monoclinic β-$(Al_xGa_{1-x})_2O_3$ alloy along different crystal orientations, high Al incorporation in pure β-phase was challenging in β-$(Al_xGa_{1-x})_2O_3$ films grown along (010) orientation. Phase segregation from β to γ with domain rotations was observed in MOCVD grown β-$(Al_xGa_{1-x})_2O_3$ films with more than 27% Al compositions [187]. Separately, n-type doping of MOCVD grown (010) β-$(Al_xGa_{1-x})_2O_3$ thin films was demonstrated by using Si as the dopant [148, 196, 199]. A controllable doping concentration from low-10^{18} cm^{-3} to low-10^{17} cm^{-3} with room temperature mobility of 42-108 cm^2/Vs was achieved for the Al compositions varied between 6.3% and 33.4% [148].

Unlike (010) oriented β-$(Al_xGa_{1-x})_2O_3$ alloy where higher Al incorporation remained challenging due to phase segregation, the (100) [195] and $(\bar{2}01)$ [193] orientations of β-Ga_2O_3 substrates showed great promise for achieving phase pure β-$(Al_xGa_{1-x})_2O_3$ films with higher Al composition. By the systematic tuning of [TMAl]/[TEGa+TMAl] molar flow ratio, chamber pressure and growth temperature, β-$(Al_xGa_{1-x})_2O_3$ films and β-$(Al_xGa_{1-x})_2O_3$/β-Ga_2O_3 SLs with Al compositions up to 52% were achieved by MOCVD on on-axis (100) β-Ga_2O_3 substrates [195]. The bandgap energies of (100) β-$(Al_xGa_{1-x})_2O_3$ range between 4.83 ± 0.12 eV (β-Ga_2O_3) and 5.85 ± 0.08 eV (β-$(Al_{0.52}Ga_{0.48})_2O_3$). The MOCVD growth of β-$(Al_xGa_{1-x})_2O_3$ films on $(\bar{2}01)$ oriented β-Ga_2O_3 substrates also revealed high-Al incorporation ($x \leqslant 0.48$) in pure β-phase [193]. Although nonuniform Al distribution was observed in $(\bar{2}01)$ β-$(Al_xGa_{1-x})_2O_3$ films, the materials were found to maintain β-phase without phase segregations or domain rotations.

Owing to the highly asymmetric crystalline structure of monoclinic β-Ga_2O_3 with three unequal axis lengths, the maximum Al incorporation in MOCVD β-$(Al_xGa_{1-x})_2O_3$ thin films grown on different surface planes of β-Ga_2O_3 substrates exhibited a strong orientation dependency. Previous studies on the MBE growth also showed highly orientation dependent Al incorporation in β-$(Al_xGa_{1-x})_2O_3$ films grown on different planes of β-Ga_2O_3 substrates. The maximum Al incorporation of 62% was achieved on (100) oriented β-Ga_2O_3 substrates [203], whereas (001) and (010) oriented β-$(Al_xGa_{1-x})_2O_3$ films exhibited maximum Al compositions of 15% [204] and ~20% [201], respectively. Similarly, MOCVD epitaxial growth of β-$(Al_xGa_{1-x})_2O_3$ thin films using TEGa as Ga precursor also shows maximum Al incorporation along (100) orientation (up to $x < 52\%$), whereas the (001) oriented β-$(Al_xGa_{1-x})_2O_3$ films showed relatively lower Al incorporation up to < 25% [148, 187, 195, 198, 205, 206], indicating a strong influence of substrate planes on the maximum Al incorporation in β-phase. Our recent investigation on MOCVD development of β-$(Al_xGa_{1-x})_2O_3$ films with different crystal orientations using TMGa as the source of Ga has yielded even higher Al compositions, surpassing 90% [207]. This finding suggests that the incorporation of Al is also strongly influenced by the choice of metalorganic precursors. A recent STEM study revealed that 54% of Al in $(Al_xGa_{1-x})_2O_3$ thin films grown on (010) β-Ga_2O_3 substrate substitutes on the octahedrally coordinated Ga_2 site [188]. While DFT calculations show that Al prefers the octahedral site, its occupancy of both octahedral and tetrahedral sites is strongly influenced by surface reconstructions and kinetic restrictions during epitaxial growth, ultimately reducing the β-phase

stability for x < ~50% [188]. Increasing Al compositions above ~27% in (010) oriented $(Al_xGa_{1-x})_2O_3$ films resulted in β-phase to γ-phase transformation [187]. Local heterogeneity in (010) $(Al_xGa_{1-x})_2O_3$ films leads to the formation of planar defect perpendicular to the growth direction when the local Al concentration reaches a critical value of ~50% that further impacts the β-phase stability [188]. At higher Al concentrations, the planar defect becomes increasingly favorable, and its formation results in a reduction of stress in the tensile strained film. In addition, $(Al_xGa_{1-x})_2O_3$ films grown on other orientations of β-Ga_2O_3 substrates, such as $(\bar{2}01)$ and (001) resulted in local segregation of Al, indicating strong influence of substrate orientations on the phase stability, alloy homogeneity and maximum Al incorporation in the films [193, 195]. We relate these experimental findings on maximum Al compositions of β-$(Al_xGa_{1-x})_2O_3$ films with the surface energy of different planes of β-Ga_2O_3 substrates. A monotonical increase of maximum Al composition in β-$(Al_xGa_{1-x})_2O_3$ films with the decrease in surface free energy of the different orientations, following the order $E_{surf\ (100)B} < E_{surf\ (-201)} < E_{surf\ (010)} < E_{surf\ (001)A}$ [208] as shown in Fig. 5. The maximum Al incorporation along (100) plane with the lowest surface free energy is much higher than along other orientations, such as (010) or (001). The presence of low density and weak dangling bonds on a very stable growth surface, for example, (100) surface results in an easier desorption of adatoms due to the lower adhesion energy on (100) terraces, causing higher reevaporation of adatoms supplied to (100) planes as compared to other planes. However, as the Al-O bonding energy is much higher than that of Ga-O bonds [209], we speculate that the reevaporation rate of Al atoms on (100) growth surface could be lower than Ga adatoms, potentially resulting in higher Al incorporation in β-$(Al_xGa_{1-x})_2O_3$ films grown on (100) plane. This indicates that the incorporation of aluminum is more favorable on planes with lower surface energy. Thus, the maximum Al incorporation in β-$(Al_xGa_{1-x})_2O_3$ films follows the order of $Al_{max\ (100)} < Al_{max\ (-201)} < Al_{max\ (010)} < Al_{max\ (001)}$, inversely following the trend of surface free energy of different planes of β-Ga_2O_3. Nevertheless, the composition of the alloy in films may also be influenced by various other factors such as growth methods and conditions, including growth temperature, chamber pressure, precursor flow rates, VI/III ratio, selection of precursors, substrate miscut directions and angles, and design of the reactor that affects the gas phase pre-reaction of the precursors.

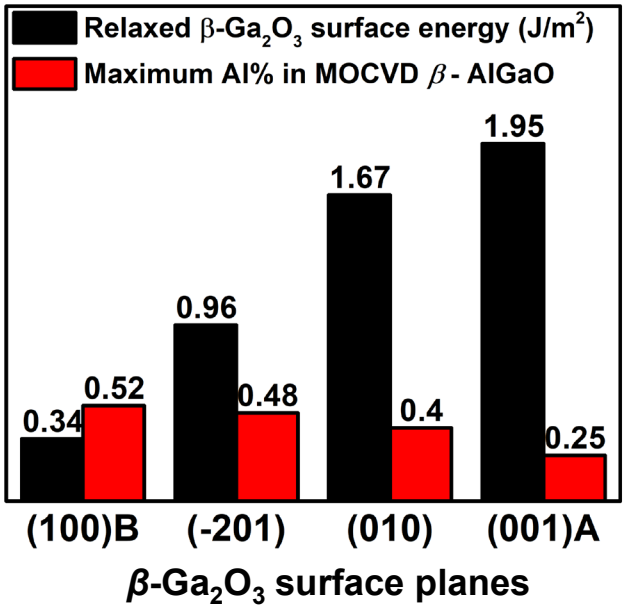

Figure 5. Relationships between the surface energies of different surface planes of β-Ga_2O_3 [208] and the maximum Al composition in MOCVD grown β-$(Al_xGa_{1-x})_2O_3$ thin films on differently oriented β-Ga_2O_3 substrates [148, 187, 193, 195, 198, 206], indicating that the substrate plane with lower surface energy promotes higher Al incorporation in phase pure β-$(Al_xGa_{1-x})_2O_3$ thin films. The β-$(Al_xGa_{1-x})_2O_3$ films are grown using TEGa as Ga precursor.

Following our studies on the MOCVD growth of β-$(Al_xGa_{1-x})_2O_3$ epitaxy on top of differently oriented β-Ga_2O_3 substrates such as (010), (100), (001) and $(\bar{2}01)$ planes which exhibited highly orientation dependent Al incorporations in β-$(Al_xGa_{1-x})_2O_3$ alloys, the band offsets at MOCVD grown β-$(Al_xGa_{1-x})_2O_3$/β-Ga_2O_3 interfaces for different orientations by varying the Al compositions are also reported [194, 200]. The valence band offsets up to -0.19±0.06 eV (x=0.52, (100)), 0.18±0.06 eV (x=0.48, $(\bar{2}01)$), -0.13±0.06 eV (x=0.35, (010)), and -0.08±0.06 eV (x=0.25, (001)) were measured. The conduction band offsets up to 1.21±0.16 eV (x=0.52, (100)), 0.76±0.20 eV (x=0.48, $(\bar{2}01)$), 0.57±0.20 eV (x=0.35, (010)), and 0.35±0.22 eV (x=0.25, (001)) were determined from the extracted bandgaps of β-Ga_2O_3 and β-$(Al_xGa_{1-x})_2O_3$ alloys with different Al compositions. The determined band offsets revealed the formation of type-II (staggered gap) heterojunctions at (100). (001) and (010) oriented β-$(Al_xGa_{1-x})_2O_3$/β-Ga_2O_3 interfaces and type I (straddling gap) heterojunction between $(\bar{2}01)$ β-Ga_2O_3 and β-$(Al_xGa_{1-x})_2O_3$ for all the Al compositions investigated. Both valence and conduction band offsets were found to increase as

the Al composition increases. The bowing parameters of 1.25 eV, 0.80 eV and 0.75 eV were extracted from the quadratic fitting of the conduction band offsets along (100), ($\bar{2}$01) and (010) orientations, respectively. The (100) orientation exhibited larger conduction band offsets as compared to (010) and ($\bar{2}$01) orientations which is consistent with theoretical DFT predictions [210].

Recently, in-situ MOCVD deposited amorphous Al_2O_3 dielectric on β-Ga_2O_3 [211, 212] and β-$(Al_xGa_{1-x})_2O_3$ [212] has been demonstrated with improved interface quality as compared to other conventional dielectric deposition techniques such as ALD and sputtering. Type II band alignments were reported at the MOCVD grown Al_2O_3/β-$(Al_xGa_{1-x})_2O_3$ interfaces with different Al compositions for (010) and (100) orientations, whereas type I band alignments with relatively lower conduction band offsets were measured along ($\bar{2}$01) orientation [212], which were found to be consistent with the band offsets at ALD deposited Al_2O_3/β-$(Al_xGa_{1-x})_2O_3$ interfaces.

In addition to the growth of β-phase $(Al_xGa_{1-x})_2O_3$ thin films, epitaxial growth of phase pure α-Ga_2O_3 and α-$(Al_xGa_{1-x})_2O_3$ for the entire Al composition range ($0 \leq x \leq 1$) on m-plane sapphire substrates are also successfully demonstrated by MOCVD [75]. The coherent growth of α-$(Al_xGa_{1-x})_2O_3$/α-Ga_2O_3 SL structures for x = 0.78 exhibited sharp interfaces and uniform Al distribution. The phase stabilization of α-Ga_2O_3 was achieved at relatively lower temperature (650°C). Bandgap energies ranging from 5.41 (x = 0) to 8.81 eV (x = 1) with a bowing parameter of 2.16 eV were determined by XPS measurement. Type I (straddling) band alignment between α-$(Al_xGa_{1-x})_2O_3$ and α-Al_2O_3 were determined for the entire Al composition range with a valance and conduction band offset of 0.27 and 3.13 eV between α-Al_2O_3 and α-Ga_2O_3.

V. Application of MOCVD Ga_2O_3 and $(Al_xGa_{1-x})_2O_3$ alloys

Recent years, progresses have been made for device demonstrations based on the MOCVD grown thin films. Ga_2O_3 MOSFET fabricated on MOCVD grown Si-doped (100) β-Ga_2O_3 was reported with device transconductance of 21 mS/mm, and extrinsic cutoff (f_T) and maximum oscillation (f_{max}) frequencies of 3.3 GHz and 12.9 GHz, respectively [213]. MOCVD-grown β-Ga_2O_3 metal-semiconductor field-effect transistor (MESFET) with improved ON-state performance has been demonstrated. The ON current value of 130 mA/mm was achieved for a depletion mode β-Ga_2O_3 MESFET with an ON-OFF ratio of over 10^{10} [214]. MOCVD grown β-Ga_2O_3 lateral MESFET showed encouraging LFOM (355 MW/cm^2), V_{BR} (~2.5 kV), and E_{AVG} (~2.5 MV/cm) [215]. In

addition, MOCVD-grown β-Ga_2O_3 vertical Schottky barrier diode (SBD) has been reported with low differential specific on-resistance of 0.67 mΩ cm^2 and Baliga's figure-of-merit (BFOM) of 0.04 GW/cm^2 using β-Ga_2O_3 drift layer (~1.1 μm) [216]. Most recently, MOCVD grown β-$(Al_xGa_{1-x})_2O_3$/β-Ga_2O_3 modulation-doped heterostructures by utilizing a delta-doped β-$(Al_xGa_{1-x})_2O_3$ (x = 20%) barrier have been demonstrated with a peak current of 22 mA/mm and on-off ratio of 8 x 10^6 [217].

VI. Conclusions and Outlook

This tutorial provides an overview on the MOCVD development of Ga_2O_3 thin films, its alloys and heterostructures. Significant progresses have been made in the past decade from bulk synthesis, thin film epitaxy, to device demonstrations. Particularly, the demonstration of high-quality β-Ga_2O_3 epitaxy by MOCVD with record high transport properties, ultra-low defect concentration, and controllable n-type doping in a wide range promises the MOCVD β-Ga_2O_3 technology for future high-performance power electronic device applications.

Nevertheless, further investigation to understand the fundamental material characteristics of MOCVD β-Ga_2O_3 such as defect states, charge compensation, and impurity incorporation is still necessary. Comprehensive defects characterization including high resolution STEM imaging, DLTS, DLOS, quantitative SIMS mapping, and electron paramagnetic resonance (EPR), together with first principle density functional theory can provide a big picture of defects identification. The development of β-Ga_2O_3 thin films for both lateral and vertical power devices will require the investigation of material epitaxy along different crystalline orientation and doping capability. For high performance vertical power devices, high quality epitaxy of thick β-Ga_2O_3 drift layers with low controllable doping concentration is required.

To address the fundamental limit of the relatively low bulk electron mobility (~200-250 cm^2/Vs) in β-Ga_2O_3 due to optical phonon scattering, the use of two-dimensional electron gas (2DEG) of $(Al_xGa_{1-x})_2O_3$/Ga_2O_3 heterostructures is expected to increase electron mobility because of the plasmon-phonon coupled dynamic screening [218]. Specifically, with the n_{2D} of 5x10^{12} cm^{-2}, the room temperature mobility is predicted to be 500 cm^2/Vs, according to the density functional theory. In order to demonstrate experimentally, epitaxy of high quality $(Al_xGa_{1-x})_2O_3$/Ga_2O_3 heterostructure with high Al composition, large band offset and smooth interfaces is still required.

Acknowledgments

The authors acknowledge the Air Force Office of Scientific Research FA9550-18-1-0479 (AFOSR, Dr. Ali Sayir) for financial support. The authors also acknowledge the National Science Foundation (No. 2231026, No. 2019753).

Data Availability Statements

The data that support the findings of this study are available from the corresponding author upon reasonable request.

References:

1. H. Tippins, Physical Review **140** (1A), A316 (1965).
2. R. Roy, V. Hill and E. Osborn, Journal of the American Chemical Society **74** (3), 719 (1952).
3. H. He, M. A. Blanco and R. Pandey, Applied physics letters **88** (26), 261904 (2006).
4. S. Yoshioka, H. Hayashi, A. Kuwabara, F. Oba, K. Matsunaga and I. Tanaka, Journal of Physics: Condensed Matter **19** (34), 346211 (2007).
5. Y. Oshima, E. G. Víllora and K. Shimamura, Applied Physics Express **8** (5), 055501 (2015).
6. M. Marezio and J. Remeika, The Journal of Chemical Physics **46** (5), 1862 (1967).
7. T. Matsumoto, M. Aoki, A. Kinoshita and T. Aono, Japanese journal of applied physics **13** (10), 1578 (1974).
8. K. Yamaguchi, Solid State Communications **131** (12), 739 (2004).
9. J. B. Varley, J. R. Weber, A. Janotti and C. G. Van de Walle, Applied Physics Letters **97** (14), 142106 (2010).
10. M. Higashiwaki, K. Sasaki, A. Kuramata, T. Masui and S. Yamakoshi, Applied Physics Letters **100** (1), 013504 (2012).
11. A. J. Green, K. D. Chabak, E. R. Heller, R. C. Fitch, M. Baldini, A. Fiedler, K. Irmscher, G. Wagner, Z. Galazka and S. E. Tetlak, IEEE Electron Device Letters **37** (7), 902 (2016).
12. K. Sasaki, M. Higashiwaki, A. Kuramata, T. Masui and S. Yamakoshi, IEEE Electron Device Lett **34** (4), 493 (2013).
13. M. Higashiwaki and G. H. Jessen, (AIP Publishing LLC, 2018), Vol. 112, pp. 060401.
14. S. J. Pearton, J. Yang, P. H. Cary, F. Ren, J. Kim, M. J. Tadjer and M. A. Mastro, Applied Physics Reviews **5** (1), 011301 (2018).
15. J. B. Varley and A. Schleife, Semiconductor Science and Technology **30** (2), 024010 (2015).
16. K. Ghosh and U. Singisetti, Journal of Applied Physics **124** (8), 085707 (2018).
17. B. J. Baliga, *Fundamentals of power semiconductor devices*. (Springer Science & Business Media, 2010).

18. C. Joishi, S. Rafique, Z. Xia, L. Han, S. Krishnamoorthy, Y. Zhang, S. Lodha, H. Zhao and S. Rajan, Applied Physics Express **11** (3), 031101 (2018).
19. Z. Xia, H. Chandrasekar, W. Moore, C. Wang, A. J. Lee, J. McGlone, N. K. Kalarickal, A. Arehart, S. Ringel, F. Yang and S. Rajan, Applied Physics Letters **115** (25), 252104 (2019).
20. N. Ma, N. Tanen, A. Verma, Z. Guo, T. Luo, H. Xing and D. Jena, Applied Physics Letters **109** (21), 212101 (2016).
21. K. Hirakawa and H. Sakaki, Physical Review B **33** (12), 8291 (1986).
22. B. Ridley, B. Foutz and L. Eastman, Physical Review B **61** (24), 16862 (2000).
23. K. Ghosh and U. Singisetti, Applied Physics Letters **109** (7), 072102 (2016).
24. Y. Kang, K. Krishnaswamy, H. Peelaers and C. G. Van de Walle, Journal of Physics: Condensed Matter **29** (23), 234001 (2017).
25. T. Onuma, S. Saito, K. Sasaki, K. Goto, T. Masui, T. Yamaguchi, T. Honda, A. Kuramata and M. Higashiwaki, Applied Physics Letters **108** (10), 101904 (2016).
26. B. J. Baliga, IEEE Electron Device Letters **10** (10), 455 (1989).
27. E. O. Johnson, in *Semiconductor Devices: Pioneering Papers* (World Scientific, 1991), pp. 295-302.
28. K. Ghosh and U. Singisetti, Journal of Applied Physics **122** (3), 035702 (2017).
29. M. Higashiwaki, K. Sasaki, H. Murakami, Y. Kumagai, A. Koukitu, A. Kuramata, T. Masui and S. Yamakoshi, Semiconductor Science and Technology **31** (3), 034001 (2016).
30. D. Guo, Q. Guo, Z. Chen, Z. Wu, P. Li and W. Tang, Materials Today Physics **11**, 100157 (2019).
31. J. Tsao, S. Chowdhury, M. Hollis, D. Jena, N. Johnson, K. Jones, R. Kaplar, S. Rajan, C. Van de Walle and E. Bellotti, Advanced Electronic Materials **4** (1), 1600501 (2018).
32. M. Baldini, M. Albrecht, A. Fiedler, K. Irmscher, R. Schewski and G. Wagner, ECS Journal of Solid State Science and Technology **6** (2), Q3040 (2016).
33. K. Goto, K. Konishi, H. Murakami, Y. Kumagai, B. Monemar, M. Higashiwaki, A. Kuramata and S. Yamakoshi, Thin Solid Films **666**, 182 (2018).
34. S. Rafique, L. Han, A. T. Neal, S. Mou, J. Boeckl and H. Zhao, physica status solidi (a) **215** (2), 1700467 (2018).
35. K. D. Leedy, K. D. Chabak, V. Vasilyev, D. C. Look, J. J. Boeckl, J. L. Brown, S. E. Tetlak, A. J. Green, N. A. Moser and A. Crespo, Applied Physics Letters **111** (1), 012103 (2017).
36. E. Ahmadi, O. S. Koksaldi, S. W. Kaun, Y. Oshima, D. B. Short, U. K. Mishra and J. S. Speck, Applied Physics Express **10** (4), 041102 (2017).
37. Y. Zhang, F. Alema, A. Mauze, O. S. Koksaldi, R. Miller, A. Osinsky and J. S. Speck, APL Materials **7** (2), 022506 (2019).
38. Y. Tomm, P. Reiche, D. Klimm and T. Fukuda, Journal of crystal growth **220** (4), 510 (2000).
39. Z. Galazka, R. Uecker, K. Irmscher, M. Albrecht, D. Klimm, M. Pietsch, M. Brützam, R. Bertram, S. Ganschow and R. Fornari, Crystal Research and Technology **45** (12), 1229 (2010).
40. H. Aida, K. Nishiguchi, H. Takeda, N. Aota, K. Sunakawa and Y. Yaguchi, Japanese Journal of Applied Physics **47** (11R), 8506 (2008).
41. A. Kuramata, K. Koshi, S. Watanabe, Y. Yamaoka, T. Masui and S. Yamakoshi, Japanese Journal of Applied Physics **55** (12), 1202A2 (2016).
42. V. Vasyltsiv, Y. I. Rym and Y. M. Zakharko, physica status solidi (b) **195** (2), 653 (1996).
43. N. Ueda, H. Hosono, R. Waseda and H. Kawazoe, Applied Physics Letters **71** (7), 933 (1997).

44. Z. Galazka, R. Uecker, D. Klimm, K. Irmscher, M. Naumann, M. Pietsch, A. Kwasniewski, R. Bertram, S. Ganschow and M. Bickermann, ECS Journal of Solid State Science and Technology **6** (2), Q3007 (2016).
45. K. Hoshikawa, E. Ohba, T. Kobayashi, J. Yanagisawa, C. Miyagawa and Y. Nakamura, Journal of Crystal Growth **447**, 36 (2016).
46. A. Kuramata, IWGO 2019 (2019).
47. S. B. Reese, T. Remo, J. Green and A. Zakutayev, Joule **3** (4), 903 (2019).
48. J. L. Lyons, Semiconductor science and technology **33** (5), 05LT02 (2018).
49. A. T. Neal, S. Mou, S. Rafique, H. Zhao, E. Ahmadi, J. S. Speck, K. T. Stevens, J. D. Blevins, D. B. Thomson, N. Moser, K. D. Chabak and G. H. Jessen, Applied Physics Letters **113** (6), 062101 (2018).
50. J. B. Varley, A. Janotti, C. Franchini and C. G. Van de Walle, Physical Review B **85** (8), 081109 (2012).
51. Z. Hu, K. Nomoto, W. Li, N. Tanen, K. Sasaki, A. Kuramata, T. Nakamura, D. Jena and H. G. Xing, IEEE Electron Device Letters **39** (6), 869 (2018).
52. W. Li, K. Nomoto, Z. Hu, D. Jena and H. G. Xing, IEEE Electron Device Letters **41** (1), 107 (2019).
53. Y. Kokubun, S. Kubo and S. Nakagomi, Applied Physics Express **9** (9), 091101 (2016).
54. J. Zhang, S. Han, M. Cui, X. Xu, W. Li, H. Xu, C. Jin, M. Gu, L. Chen and K. H. Zhang, ACS Applied Electronic Materials **2** (2), 456 (2020).
55. W. Hao, Q. He, K. Zhou, G. Xu, W. Xiong, X. Zhou, G. Jian, C. Chen, X. Zhao and S. Long, Applied Physics Letters **118** (4), 043501 (2021).
56. S.-i. Kan, S. Takemoto, K. Kaneko, I. Takahashi, M. Sugimoto, T. Shinohe and S. Fujita, Applied Physics Letters **113** (21), 212104 (2018).
57. K. Kaneko, Y. Masuda, S.-i. Kan, I. Takahashi, Y. Kato, T. Shinohe and S. Fujita, Applied Physics Letters **118** (10), 102104 (2021).
58. Z. Guo, A. Verma, X. Wu, F. Sun, A. Hickman, T. Masui, A. Kuramata, M. Higashiwaki, D. Jena and T. Luo, Applied Physics Letters **106** (11), 111909 (2015).
59. M. J. Tadjer, The Electrochemical Society Interface **27** (4), 49 (2018).
60. J. Pomeroy, C. Middleton, M. Singh, S. Dalcanale, M. Uren, M. Wong, K. Sasaki, A. Kuramata, S. Yamakoshi and M. Higashiwaki, IEEE Electron Device Letters **40** (2), 189 (2018).
61. B. Chatterjee, K. Zeng, C. D. Nordquist, U. Singisetti and S. Choi, IEEE Transactions on Components, Packaging and Manufacturing Technology **9** (12), 2352 (2019).
62. J. Zhang, J. Shi, D.-C. Qi, L. Chen and K. H. Zhang, APL Materials **8** (2), 020906 (2020).
63. S. Stepanov, V. Nikolaev, V. Bougrov and A. Romanov, Rev. Adv. Mater. Sci **44**, 63 (2016).
64. B. R. Tak, S. Kumar, A. K. Kapoor, D. Wang, X. Li, H. Sun and R. Singh, Journal of Physics D: Applied Physics **54** (45), 453002 (2021).
65. M. Bosi, P. Mazzolini, L. Seravalli and R. Fornari, Journal of Materials Chemistry C **8** (32), 10975 (2020).
66. J. Xu, W. Zheng and F. Huang, Journal of Materials Chemistry C **7** (29), 8753 (2019).
67. M. Biswas and H. Nishinaka, APL Materials **10** (6), 060701 (2022).
68. K. Kaneko, K. Uno, R. Jinno and S. Fujita, Journal of Applied Physics **131** (9) (2022).
69. H. Peelaers, J. B. Varley, J. S. Speck and C. G. Van de Walle, Applied Physics Letters **112** (24), 242101 (2018).

70. A F M A. U. Bhuiyan, Z. Feng, H.-L. Huang, L. Meng, J. Hwang and H. Zhao, Journal of Vacuum Science & Technology A **40** (6) (2022).
71. I. Cora, F. Mezzadri, F. Boschi, M. Bosi, M. Čaplovičová, G. Calestani, I. Dódony, B. Pécz and R. Fornari, CrystEngComm **19** (11), 1509 (2017).
72. M. B. Maccioni and V. Fiorentini, Applied Physics Express **9** (4), 041102 (2016).
73. H. Y. Playford, A. C. Hannon, M. G. Tucker, D. M. Dawson, S. E. Ashbrook, R. J. Kastiban, J. Sloan and R. I. Walton, The Journal of Physical Chemistry C **118** (29), 16188 (2014).
74. T. Kato, H. Nishinaka, K. Shimazoe, K. Kanegae and M. Yoshimoto, ACS Applied Electronic Materials **5** (3), 1715 (2023).
75. A F M A. U. Bhuiyan, Z. Feng, H.-L. Huang, L. Meng, J. Hwang and H. Zhao, APL Materials **9** (10), 101109 (2021).
76. K. Uno, M. Ohta and I. Tanaka, Applied Physics Letters **117** (5) (2020).
77. Y. Cheng, Y. Xu, Z. Li, J. Zhang, D. Chen, Q. Feng, S. Xu, H. Zhou, J. Zhang, Y. Hao and C. Zhang, Journal of Alloys and Compounds **831**, 154776 (2020).
78. U. U. Muazzam, P. Chavan, S. Raghavan, R. Muralidharan and D. N. Nath, IEEE Photonics Technology Letters **32** (7), 422 (2020).
79. R. Jinno, C. S. Chang, T. Onuma, Y. Cho, S. T. Ho, D. Rowe, M. C. Cao, K. Lee, V. Protasenko, D. G. Schlom, D. A. Muller, H. G. Xing and D. Jena, Sci Adv **7** (2) (2021).
80. A. Y. Polyakov, V. I. Nikolaev, S. I. Stepanov, A. I. Pechnikov, E. B. Yakimov, N. B. Smirnov, I. V. Shchemerov, A. A. Vasilev, A. I. Kochkova, A. V. Chernykh and S. J. Pearton, ECS Journal of Solid State Science and Technology **9** (4), 045003 (2020).
81. V. D. Wheeler, N. Nepal, D. R. Boris, S. B. Qadri, L. O. Nyakiti, A. Lang, A. Koehler, G. Foster, S. G. Walton, C. R. Eddy and D. J. Meyer, Chemistry of Materials **32** (3), 1140 (2020).
82. D. Shinohara and S. Fujita, Japanese Journal of Applied Physics **47** (9R), 7311 (2008).
83. Z. Feng, A F M A. U. Bhuiyan, M. R. Karim and H. Zhao, Applied Physics Letters **114** (25), 250601 (2019).
84. Z. Feng, A F M A. U. Bhuiyan, Z. Xia, W. Moore, Z. Chen, J. F. McGlone, D. R. Daughton, A. R. Arehart, S. A. Ringel, S. Rajan and H. Zhao, physica status solidi (RRL) – Rapid Research Letters **14** (8), 2000145 (2020).
85. Z. Feng, A F M A. U. Bhuiyan, N. K. Kalarickal, S. Rajan and H. Zhao, Applied Physics Letters **117** (22), 222106 (2020).
86. L. Meng, A F M A. U. Bhuiyan, Z. Feng, H.-L. Huang, J. Hwang and H. Zhao, Journal of Vacuum Science & Technology A **40** (6) (2022).
87. K. Sasaki, A. Kuramata, T. Masui, E. G. Villora, K. Shimamura and S. Yamakoshi, Applied Physics Express **5** (3), 035502 (2012).
88. K. Sasaki, M. Higashiwaki, A. Kuramata, T. Masui and S. Yamakoshi, Journal of Crystal Growth **392**, 30 (2014).
89. K. Azizie, F. V. E. Hensling, C. A. Gorsak, Y. Kim, N. A. Pieczulewski, D. M. Dryden, M. K. I. Senevirathna, S. Coye, S.-L. Shang, J. Steele, P. Vogt, N. A. Parker, Y. A. Birkhölzer, J. P. McCandless, D. Jena, H. G. Xing, Z.-K. Liu, M. D. Williams, A. J. Green, K. Chabak, D. A. Muller, A. T. Neal, S. Mou, M. O. Thompson, H. P. Nair and D. G. Schlom, APL Materials **11** (4) (2023).
90. J. P. McCandless, V. Protasenko, B. W. Morell, E. Steinbrunner, A. T. Neal, N. Tanen, Y. Cho, T. J. Asel, S. Mou, P. Vogt, H. G. Xing and D. Jena, Applied Physics Letters **121** (7) (2022).

91. J. H. Leach, K. Udwary, J. Rumsey, G. Dodson, H. Splawn and K. R. Evans, APL Materials **7** (2) (2018).
92. H. Murakami, K. Nomura, K. Goto, K. Sasaki, K. Kawara, Q. T. Thieu, R. Togashi, Y. Kumagai, M. Higashiwaki and A. Kuramata, Applied Physics Express **8** (1), 015503 (2014).
93. S.-d. Lee, K. Kaneko and S. Fujita, Japanese Journal of Applied Physics **55** (12), 1202B8 (2016).
94. S. Rafique, L. Han, A. T. Neal, S. Mou, M. J. Tadjer, R. H. French and H. Zhao, Applied Physics Letters **109** (13), 132103 (2016).
95. S. Rafique, L. Han, M. J. Tadjer, J. A. Freitas, N. A. Mahadik and H. Zhao, Applied Physics Letters **108** (18), 182105 (2016).
96. C. X. Xu, H. Liu, X. H. Pan and Z. Z. Ye, Optical Materials **108**, 110145 (2020).
97. S. Ghosh, H. Srivastava, P. N. Rao, M. Nand, P. Tiwari, A. K. Srivastava, S. N. Jha, S. K. Rai, S. D. Singh and T. Ganguli, Semiconductor Science and Technology **35** (8), 085024 (2020).
98. P. Mazzolini and O. Bierwagen, Journal of Physics D: Applied Physics **53** (35), 354003 (2020).
99. S. B. Anooz, R. Grüneberg, C. Wouters, R. Schewski, M. Albrecht, A. Fiedler, K. Irmscher, Z. Galazka, W. Miller, G. Wagner, J. Schwarzkopf and A. Popp, Applied Physics Letters **116** (18), 182106 (2020).
100. F. Alema, Y. Zhang, A. Osinsky, N. Orishchin, N. Valente, A. Mauze and J. S. Speck, APL Materials **8** (2), 021110 (2020).
101. T. Oshima, T. Nakazono, A. Mukai and A. Ohtomo, Journal of Crystal Growth **359**, 60 (2012).
102. F. Boschi, M. Bosi, T. Berzina, E. Buffagni, C. Ferrari and R. Fornari, Journal of Crystal Growth **443**, 25 (2016).
103. X. Xia, Y. Chen, Q. Feng, H. Liang, P. Tao, M. Xu and G. Du, Applied Physics Letters **108** (20), 202103 (2016).
104. F. Mezzadri, G. Calestani, F. Boschi, D. Delmonte, M. Bosi and R. Fornari, Inorg Chem **55** (22), 12079 (2016).
105. K. Jiang, J. Tang, M. J. Cabral, A. Park, L. Gu, R. F. Davis and L. M. Porter, Journal of Applied Physics **131** (5), 055305 (2022).
106. Y. Oshima, E. G. Víllora, Y. Matsushita, S. Yamamoto and K. Shimamura, Journal of Applied Physics **118** (8), 085301 (2015).
107. Y. Yao, S. Okur, L. A. M. Lyle, G. S. Tompa, T. Salagaj, N. Sbrockey, R. F. Davis and L. M. Porter, Materials Research Letters **6** (5), 268 (2018).
108. D. Tahara, H. Nishinaka, S. Morimoto and M. Yoshimoto, Japanese Journal of Applied Physics **56** (7), 078004 (2017).
109. H. Nishinaka, D. Tahara and M. Yoshimoto, Japanese Journal of Applied Physics **55** (12), 1202BC (2016).
110. P. Vogt, O. Brandt, H. Riechert, J. Lähnemann and O. Bierwagen, Physical review letters **119** (19), 196001 (2017).
111. M. Kneiß, A. Hassa, D. Splith, C. Sturm, H. von Wenckstern, T. Schultz, N. Koch, M. Lorenz and M. Grundmann, APL Materials **7** (2), 022516 (2019).
112. M. Kracht, A. Karg, J. Schörmann, M. Weinhold, D. Zink, F. Michel, M. Rohnke, M. Schowalter, B. Gerken, A. Rosenauer, P. J. Klar, J. Janek and M. Eickhoff, Physical Review Applied **8** (5), 054002 (2017).
113. Y. Oshima, E. G. Víllora and K. Shimamura, Journal of Crystal Growth **410**, 53 (2015).

114. K. Nomura, K. Goto, R. Togashi, H. Murakami, Y. Kumagai, A. Kuramata, S. Yamakoshi and A. Koukitu, Journal of crystal growth **405**, 19 (2014).
115. V. Nikolaev, A. Pechnikov, S. Stepanov, I. Nikitina, A. Smirnov, A. Chikiryaka, S. Sharofidinov, V. Bougrov and A. Romanov, Materials Science in Semiconductor Processing **47**, 16 (2016).
116. V. Nikolaev, A. Pechnikov, V. Nikolaev, M. Scheglov, A. Chikiryaka, S. Stepanov, O. Medvedev, S. Shapenkov, E. Ubyivovk and O. Vyvenko, presented at the Journal of Physics: Conference Series, 2019 (unpublished).
117. M.-Y. Tsai, O. Bierwagen, M. E. White and J. S. Speck, Journal of Vacuum Science & Technology A: Vacuum, Surfaces, and Films **28** (2), 354 (2010).
118. P. Vogt and O. Bierwagen, Applied Physics Letters **108** (7), 072101 (2016).
119. Z. Xia, C. Joishi, S. Krishnamoorthy, S. Bajaj, Y. Zhang, M. Brenner, S. Lodha and S. Rajan, IEEE Electron Device Letters **39** (4), 568 (2018).
120. N. K. Kalarickal, Z. Xia, J. McGlone, S. Krishnamoorthy, W. Moore, M. Brenner, A. R. Arehart, S. A. Ringel and S. Rajan, Applied Physics Letters **115** (15), 152106 (2019).
121. P. Mazzolini, A. Falkenstein, C. Wouters, R. Schewski, T. Markurt, Z. Galazka, M. Martin, M. Albrecht and O. Bierwagen, APL Materials **8** (1), 011107 (2020).
122. A. Mauze, Y. Zhang, T. Itoh, F. Wu and J. S. Speck, APL Materials **8** (2), 021104 (2020).
123. P. Vogt, F. V. E. Hensling, K. Azizie, C. S. Chang, D. Turner, J. Park, J. P. McCandless, H. Paik, B. J. Bocklund, G. Hoffman, O. Bierwagen, D. Jena, H. G. Xing, S. Mou, D. A. Muller, S.-L. Shang, Z.-K. Liu and D. G. Schlom, APL Materials **9** (3) (2021).
124. Y. Zhang, A. Neal, Z. Xia, C. Joishi, J. M. Johnson, Y. Zheng, S. Bajaj, M. Brenner, D. Dorsey, K. Chabak, G. Jessen, J. Hwang, S. Mou, J. P. Heremans and S. Rajan, Applied Physics Letters **112** (17), 173502 (2018).
125. Y. Zhang, C. Joishi, Z. Xia, M. Brenner, S. Lodha and S. Rajan, Applied Physics Letters **112** (23), 233503 (2018).
126. H. Ito, K. Kaneko and S. Fujita, Japanese Journal of Applied Physics **51**, 100207 (2012).
127. K. Akaiwa and S. Fujita, Japanese Journal of Applied Physics **51**, 070203 (2012).
128. K. Akaiwa, K. Kaneko, K. Ichino and S. Fujita, Japanese Journal of Applied Physics **55** (12), 1202BA (2016).
129. S. Rafique, L. Han and H. Zhao, physica status solidi (a) **213** (4), 1002 (2016).
130. S. Rafique, L. Han, S. Mou and H. Zhao, Optical Materials Express **7** (10), 3561 (2017).
131. S. Rafique, M. R. Karim, J. M. Johnson, J. Hwang and H. Zhao, Applied Physics Letters **112** (5), 052104 (2018).
132. Z. Feng, M. R. Karim and H. Zhao, APL Materials **7** (2), 022514 (2019).
133. Y. Zhang, M. R. Karim, Z. Feng and H. Zhao, Journal of Applied Physics **125** (13), 135703 (2019).
134. S. Saha, L. Meng, Z. Feng, A F M A. U. Bhuiyan, H. Zhao and U. Singisetti, Applied Physics Letters **120** (12), 122106 (2022).
135. M. R. Karim, Z. Feng and H. Zhao, Crystal Growth & Design **18** (8), 4495 (2018).
136. C. Kranert, J. Lenzner, M. Jenderka, M. Lorenz, H. v. Wenckstern, R. Schmidt-Grund and M. Grundmann, Journal of Applied Physics **116** (1), 013505 (2014).
137. H. v. Wenckstern, D. Splith, M. Purfürst, Z. Zhang, C. Kranert, S. Müller, M. Lorenz and M. Grundmann, Semiconductor Science and Technology **30** (2), 024005 (2015).
138. M. Kneiß, A. Hassa, D. Splith, C. Sturm, H. v. Wenckstern, M. Lorenz and M. Grundmann, APL Materials **7** (10), 101102 (2019).

139. D. J. Comstock and J. W. Elam, Chemistry of Materials **24** (21), 4011 (2012).
140. R. K. Ramachandran, J. Dendooven, J. Botterman, S. Pulinthanathu Sree, D. Poelman, J. A. Martens, H. Poelman and C. Detavernier, Journal of Materials Chemistry A **2** (45), 19232 (2014).
141. A. K. Chandiran, N. Tetreault, R. Humphry-Baker, F. Kessler, E. Baranoff, C. Yi, M. K. Nazeeruddin and M. Grätzel, Nano Letters **12** (8), 3941 (2012).
142. G. Seryogin, F. Alema, N. Valente, H. Fu, E. Steinbrunner, A. T. Neal, S. Mou, A. Fine and A. Osinsky, Applied Physics Letters **117** (26), 262101 (2020).
143. F. Alema, Y. Zhang, A. Mauze, T. Itoh, J. S. Speck, B. Hertog and A. Osinsky, AIP Advances **10** (8), 085002 (2020).
144. F. Alema, G. Seryogin, A. Osinsky and A. Osinsky, APL Materials **9** (9), 091102 (2021).
145. F. Alema, B. Hertog, A. Osinsky, P. Mukhopadhyay, M. Toporkov and W. V. Schoenfeld, Journal of Crystal Growth **475**, 77 (2017).
146. L. Meng, Z. Feng, A F M A. U. Bhuiyan and H. Zhao, Crystal Growth & Design **22** (6), 3896 (2022).
147. F. Alema, Y. Zhang, A. Osinsky, N. Valente, A. Mauze, T. Itoh and J. S. Speck, APL Materials **7** (12) (2019).
148. A F M A. U. Bhuiyan, Z. Feng, J. M. Johnson, Z. Chen, H.-L. Huang, J. Hwang and H. Zhao, Applied Physics Letters **115** (12), 120602 (2019).
149. H. Ghadi, J. F. McGlone, C. M. Jackson, E. Farzana, Z. Feng, A F M A. U. Bhuiyan, H. Zhao, A. R. Arehart and S. A. Ringel, APL Materials **8** (2), 021111 (2020).
150. H. Ghadi, J. F. McGlone, Z. Feng, A F M A. U. Bhuiyan, H. Zhao, A. R. Arehart and S. A. Ringel, Applied Physics Letters **117** (17), 172106 (2020).
151. A. Bhattacharyya, P. Ranga, S. Roy, J. Ogle, L. Whittaker-Brooks and S. Krishnamoorthy, Applied Physics Letters **117** (14), 142102 (2020).
152. A. Bhattacharyya, C. Peterson, T. Itoh, S. Roy, J. Cooke, S. Rebollo, P. Ranga, B. Sensale-Rodriguez and S. Krishnamoorthy, APL Materials **11** (2), 021110 (2023).
153. R. Schewski, K. Lion, A. Fiedler, C. Wouters, A. Popp, S. V. Levchenko, T. Schulz, M. Schmidbauer, S. Bin Anooz, R. Grüneberg, Z. Galazka, G. Wagner, K. Irmscher, M. Scheffler, C. Draxl and M. Albrecht, APL Materials **7** (2), 022515 (2019).
154. R. Schewski, M. Baldini, K. Irmscher, A. Fiedler, T. Markurt, B. Neuschulz, T. Remmele, T. Schulz, G. Wagner, Z. Galazka and M. Albrecht, Journal of Applied Physics **120** (22), 225308 (2016).
155. V. Gottschalch, K. Mergenthaler, G. Wagner, J. Bauer, H. Paetzelt, C. Sturm and U. Teschner, physica status solidi (a) **206** (2), 243 (2009).
156. D. Gogova, G. Wagner, M. Baldini, M. Schmidbauer, K. Irmscher, R. Schewski, Z. Galazka, M. Albrecht and R. Fornari, Journal of Crystal Growth **401**, 665 (2014).
157. D. Gogova, M. Schmidbauer and A. Kwasniewski, CrystEngComm **17** (35), 6744 (2015).
158. H. W. Kim and N. H. Kim, Materials Science and Engineering: B **110** (1), 34 (2004).
159. D. Gogova, M. Ghezellou, D. Q. Tran, S. Richter, A. Papamichail, J. u. Hassan, A. R. Persson, P. O. Å. Persson, O. Kordina, B. Monemar, M. Hilfiker, M. Schubert, P. P. Paskov and V. Darakchieva, AIP Advances **12** (5) (2022).
160. M. Baldini, D. Gogova, K. Irmscher, M. Schmidbauer, G. Wagner and R. Fornari, Crystal Research and Technology **49** (8), 552 (2014).
161. Y. Song, P. Ranga, Y. Zhang, Z. Feng, H.-L. Huang, M. D. Santia, S. C. Badescu, C. U. Gonzalez-Valle, C. Perez, K. Ferri, R. M. Lavelle, D. W. Snyder, B. A. Klein, J. Deitz, A. G. Baca, J.-P.

Maria, B. Ramos-Alvarado, J. Hwang, H. Zhao, X. Wang, S. Krishnamoorthy, B. M. Foley and S. Choi, ACS Applied Materials & Interfaces **13** (32), 38477 (2021).
162. Y. Chen, H. Liang, X. Xia, P. Tao, R. Shen, Y. Liu, Y. Feng, Y. Zheng, X. Li and G. Du, Journal of Materials Science: Materials in Electronics **26** (5), 3231 (2015).
163. G. Stringfellow, Journal of Crystal Growth **68** (1), 111 (1984).
164. J. O. Williams, Angewandte Chemie International Edition in English **28** (8), 1110 (1989).
165. M. E. Pemble, D. S. Buhaenko, S. M. Francis, P. A. Goulding and J. T. Allen, Journal of crystal growth **107** (1-4), 37 (1991).
166. G. B. Stringfellow, *Organometallic vapor-phase epitaxy: theory and practice*. (Elsevier, 1999).
167. K. F. Jensen, D. I. Fotiadis and T. J. Mountziaris, Journal of crystal growth **107** (1-4), 1 (1991).
168. C. Larsen, N. Buchan and G. Stringfellow, Applied physics letters **52** (6), 480 (1988).
169. D. V. Shenai-Khatkhate, R. J. Goyette, R. L. DiCarlo Jr and G. Dripps, Journal of Crystal Growth **272** (1), 816 (2004).
170. S. Irvine and P. Capper, *Metalorganic vapor phase epitaxy (MOVPE): Growth, materials properties, and applications*. (John Wiley & Sons, 2019).
171. M. Baldini, M. Albrecht, A. Fiedler, K. Irmscher, D. Klimm, R. Schewski and G. Wagner, Journal of Materials Science **51** (7), 3650 (2016).
172. K.-H. Lee, P.-C. Chang, S.-J. Chang, Y.-K. Su, S.-L. Wu and M. Pilkuhn, Materials Chemistry and Physics **134** (2), 899 (2012).
173. K. Goto, K. Ikenaga, N. Tanaka, M. Ishikawa, H. Machida and Y. Kumagai, Japanese Journal of Applied Physics **60** (4), 045505 (2021).
174. M. Yoshida, H. Watanabe and F. Uesugi, Journal of The Electrochemical Society **132** (3), 677 (1985).
175. C. A. Larsen, N. I. Buchan, S. H. Li and G. B. Stringfellow, Journal of Crystal Growth **102** (1), 103 (1990).
176. G. S. Bales, Surface Science **356** (1), L439 (1996).
177. S. Bin Anooz, R. Grüneberg, T. S. Chou, A. Fiedler, K. Irmscher, C. Wouters, R. Schewski, M. Albrecht, Z. Galazka, W. Miller, J. Schwarzkopf and A. Popp, Journal of Physics D: Applied Physics **54** (3), 034003 (2021).
178. A. Waseem, Z. Ren, H.-C. Huang, K. Nguyen, X. Wu and X. Li, physica status solidi (a) **220** (8), 2200616 (2023).
179. T.-S. Chou, P. Seyidov, S. B. Anooz, R. Grüneberg, M. Pietsch, J. Rehm, T. T. V. Tran, K. Tetzner, Z. Galazka, M. Albrecht, K. Irmscher, A. Fiedler and A. Popp, Applied Physics Letters **122** (5), 052102 (2023).
180. T.-S. Chou, P. Seyidov, S. B. Anooz, R. Grüneberg, T. T. V. Tran, K. Irmscher, M. Albrecht, Z. Galazka, J. Schwarzkopf and A. Popp, AIP Advances **11** (11), 115323 (2021).
181. V. Gottschalch, S. Merker, S. Blaurock, M. Kneiß, U. Teschner, M. Grundmann and H. Krautscheid, Journal of Crystal Growth **510**, 76 (2019).
182. H. Sun, K.-H. Li, C. G. T. Castanedo, S. Okur, G. S. Tompa, T. Salagaj, S. Lopatin, A. Genovese and X. Li, Crystal Growth & Design **18** (4), 2370 (2018).
183. T. Kawaharamura, G. T. Dang and M. Furuta, Japanese Journal of Applied Physics **51** (4R), 040207 (2012).
184. K. Akaiwa, K. Ota, T. Sekiyama, T. Abe, T. Shinohe and K. Ichino, physica status solidi (a) **217** (3), 1900632 (2020).

185. Y. Lv, W. Mi, C. N. Luan and J. Ma, Advanced Materials Research **746**, 369 (2013).
186. C. S. Chang, N. Tanen, V. Protasenko, T. J. Asel, S. Mou, H. G. Xing, D. Jena and D. A. Muller, APL Materials **9** (5), 051119 (2021).
187. A F M A. U. Bhuiyan, Z. Feng, J. M. Johnson, H.-L. Huang, J. Sarker, M. Zhu, M. R. Karim, B. Mazumder, J. Hwang and H. Zhao, APL Materials **8** (3), 031104 (2020).
188. J. M. Johnson, H.-L. Huang, M. Wang, S. Mu, J. B. Varley, A F M A. U. Bhuiyan, Z. Feng, N. K. Kalarickal, S. Rajan, H. Zhao, C. G. Van de Walle and J. Hwang, APL Materials **9** (5), 051103 (2021).
189. J. Kim, D. Tahara, Y. Miura and B. G. Kim, Applied Physics Express **11** (6), 061101 (2018).
190. M. Bosi, L. Seravalli, P. Mazzolini, F. Mezzadri and R. Fornari, Crystal Growth & Design **21** (11), 6393 (2021).
191. Y. Chen, X. Xia, H. Liang, Q. Abbas, Y. Liu and G. Du, Crystal Growth & Design **18** (2), 1147 (2018).
192. Y. Zhuo, Z. Chen, W. Tu, X. Ma, Y. Pei and G. Wang, Applied Surface Science **420**, 802 (2017).
193. A F M A. U. Bhuiyan, Z. Feng, J. M. Johnson, H.-L. Huang, J. Hwang and H. Zhao, Applied Physics Letters **117** (14), 142107 (2020).
194. A F M A. U. Bhuiyan, Z. Feng, J. M. Johnson, H.-L. Huang, J. Hwang and H. Zhao, Applied Physics Letters **117** (25), 252105 (2020).
195. A F M A. U. Bhuiyan , Z. Feng, J. M. Johnson, H.-L. Huang, J. Hwang and H. Zhao, Crystal Growth & Design **20** (10), 6722 (2020).
196. J. Sarker, A F M A. U. Bhuiyan, Z. Feng, H. Zhao and B. Mazumder, Journal of Physics D: Applied Physics **54** (18), 184001 (2021).
197. J. Sarker, S. Broderick, A F M A. U. Bhuiyan, Z. Feng, H. Zhao and B. Mazumder, Applied Physics Letters **116** (15), 152101 (2020).
198. A F M A. U. Bhuiyan, Z. Feng, L. Meng and H. Zhao, Journal of Materials Research **36** (23), 4804 (2021).
199. A F M A. U. Bhuiyan, Z. Feng, L. Meng, A. Fiedler, H.-L. Huang, A. T. Neal, E. Steinbrunner, S. Mou, J. Hwang, S. Rajan and H. Zhao, Journal of Applied Physics **131** (14), 145301 (2022).
200. A F M A. U. Bhuiyan, Z. Feng, H.-L. Huang, L. Meng, J. Hwang and H. Zhao, Journal of Vacuum Science & Technology A **39** (6), 063207 (2021).
201. S. W. Kaun, F. Wu and J. S. Speck, Journal of Vacuum Science & Technology A: Vacuum, Surfaces, and Films **33** (4), 041508 (2015).
202. R. Miller, F. Alema and A. Osinsky, IEEE Transactions on Semiconductor Manufacturing **31** (4), 467 (2018).
203. T. Oshima, T. Okuno, N. Arai, Y. Kobayashi and S. Fujita, Japanese Journal of Applied Physics **48** (7), 070202 (2009).
204. A. Mauze, T. Itoh, Y. Zhang, E. Deagueros, F. Wu and J. S. Speck, Journal of Applied Physics **132** (11), 115302 (2022).
205. A F M A. U. Bhuiyan , L. Meng, H.-L. Huang, J. Sarker, C. Chae, B. Mazumder, J. Hwang and H. Zhao, APL Materials **11** (4) (2023).
206. A F M A. U. Bhuiyan, Z. Feng, L. Meng, A. Fiedler, H.-L. Huang, A. T. Neal, E. Steinbrunner, S. Mou, J. Hwang, S. Rajan and H. Zhao, Journal of Applied Physics (2022).
207. A F M A. U. Bhuiyan, L. Meng, Hsien-Lien Huang, Jinwoo Hwang, and Hongping Zhao, in *6th U.S. Workshop on Gallium Oxide (GOX 2023)* (Buffalo, New York, 2023).

208. S. Mu, M. Wang, H. Peelaers and C. G. Van de Walle, APL Materials **8** (9), 091105 (2020).
209. Y. R. Luo, Bond Dissociation Energies. In CRC Handbook of Chemistry and Physics, 90th ed.; Lide, D. R., Ed.; CRC Press/Taylor and Francis,: Boca Raton, FL, 2009..
210. S. Mu, H. Peelaers, Y. Zhang, M. Wang and C. G. Van de Walle, Applied Physics Letters **117** (25), 252104 (2020).
211. S. Roy, A. E. Chmielewski, A. Bhattacharyya, P. Ranga, R. Sun, M. A. Scarpulla, N. Alem and S. Krishnamoorthy, Advanced Electronic Materials **7** (11), 2100333 (2021).
212. A F M A. U. Bhuiyan, L. Meng, H.-L. Huang, J. Hwang and H. Zhao, (2022), pp. arXiv:2207.13001.
213. A. J. Green, K. D. Chabak, M. Baldini, N. Moser, R. Gilbert, R. C. Fitch, G. Wagner, Z. Galazka, J. Mccandless, A. Crespo, K. Leedy and G. H. Jessen, IEEE Electron Device Letters **38** (6), 790 (2017).
214. A. Bhattacharyya, S. Roy, P. Ranga, D. Shoemaker, Y. Song, J. S. Lundh, S. Choi and S. Krishnamoorthy, Applied Physics Express **14** (7), 076502 (2021).
215. A. Bhattacharyya, P. Ranga, S. Roy, C. Peterson, F. Alema, G. Seryogin, A. Osinsky and S. Krishnamoorthy, IEEE Electron Device Letters **42** (9), 1272 (2021).
216. E. Farzana, F. Alema, W. Y. Ho, A. Mauze, T. Itoh, A. Osinsky and J. S. Speck, Applied Physics Letters **118** (16), 162109 (2021).
217. P. Ranga, A. Bhattacharyya, A. Chmielewski, S. Roy, R. Sun, M. A. Scarpulla, N. Alem and S. Krishnamoorthy, Applied Physics Express **14** (2), 025501 (2021).
218. A. Kumar, K. Ghosh and U. Singisetti, Journal of Applied Physics **128** (10), 105703 (2020).